Contrib Mineral Petrol (2009) 157:383–409
DOI 10.1007/s00410-008-0341-x

ORIGINAL PAPER

Late Mesozoic magmatism from the Daye region, eastern China: U–Pb ages, petrogenesis, and geodynamic implications

Jian-Wei Li · Xin-Fu Zhao · Mei-Fu Zhou · Chang-Qian Ma · Zorano Sérgio de Souza · Paulo Vasconcelos

Received: 13 March 2008 / Accepted: 29 August 2008 / Published online: 20 September 2008

Abstract Late Mesozoic dioritic and quartz dioritic plutons are widespread in the Daye region, eastern Yangtze craton, eastern China. Detailed geochronological, geochemical, and Sr–Nd isotopic studies have been undertaken for most of these plutons, in an attempt to provide a comprehensive understanding in the age, genesis and geodynamical control of the extensive magmatism. SHRIMP and LA-ICP-MS zircon U–Pb dating indicate that the plutons were emplaced in the range of latest Jurassic (ca. 152 Ma) to early Cretaceous (ca. 132 Ma), which was followed by dyke emplacement between 127 and 121 Ma and volcanism during the 130–113 Ma interval. Both diorites and quartz diorites are sodic, metaluminous, high-K calc-alkaline, and characterized by strongly fractionated, sub-parallel REE patterns without obvious Eu anomalies. The rocks are enriched in highly incompatible elements and large ion lithophile elements, but depleted in high field strength elements. Samples of diorite and quartz diorite have similar Sr–Nd isotopic compositions that are consistent with the early Cretaceous basalts and mafic intrusions throughout the eastern Yangtze craton. The geochemical and isotopic data, together with results of geochemical modeling, indicate an enriched mantle source for the plutonic rocks. The quartz diorites have geochemical signatures resembling adakites, such as high Al_2O_3 (15–19 wt.%), Sr (630–2,080 ppm), Na_2O (>3.5 wt.%), negative Nb–Ta anomalies, low Y (7–19 ppm), Yb (0.5–1.8 ppm), Sc (5–15 ppm), and resultant high Sr/Y (45–200) and La/Yb (31–63) ratios. Genesis of the adakitic quartz diorites is best explained in terms of low-pressure intracrustal fractional crystallization of cumulates consisting of hornblende, plagioclase, K-feldspar, magnetite, and apatite from mantle-derived dioritic magmas. Mantle-derived magmatism broadly coeval with that of the Daye region also is widespread in other regions of the eastern Yangtze craton, reflecting large-scale melting of the lithospheric mantle during the Late Mesozoic. The large-scale magmatism was most likely driven by lithospheric extension associated with thinning of lithospheric mantle beneath the eastern China continent.

Keywords Adakite · Fractional crystallization · Partial melting · Lithospheric extension · Yangtze craton · Eastern China

Communicated by H. Keppler.

J.-W. Li (✉) · C.-Q. Ma
State Key Laboratory of Geological Processes and Mineral Resources, China University of Geosciences, 430074 Wuhan, China
e-mail: jwli@cug.edu.cn

J.-W. Li · X.-F. Zhao
Faculty of Earth Resources, China University of Geosciences, 430074 Wuhan, China

X.-F. Zhao · M.-F. Zhou
Department of Earth Sciences, The University of Hong Kong, Hong Kong SAR, China

Z. S. de Souza
Pós-Graduação em Geodinâmica e Geofísica, Universidade Federal do Rio Grande do Norte, Natal 59078-970, Brazil

P. Vasconcelos
Department of Earth Sciences, The University of Queensland, Brisbane 4072, Australia

Introduction

Widespread Late Mesozoic plutonic and volcanic rocks that range in composition from mafic to acidic characterize

the eastern Yangtze craton, eastern China. The magmatism has been traditionally thought to be related to the subduction of the paleo-Pacific plate underneath the eastern China continent (Zhou and Li 2000; Li and Li 2007). On the contrary, Zhai et al. (1996) proposed that a continental rift setting was responsible for the magmatism. Recent investigations have led to recognition of a number of adakitic intrusions over the eastern Yangtze craton, whose origin has been interpreted as derivation from partial melting of a thickened lower crust or delaminated lower crust in the lithospheric mantle (Xu et al. 2002; Wang et al. 2004, 2006).

The Daye region represents the westernmost and largest magmatic region within the eastern Yangtze craton (Fig. 1). Previous isotopic dating, mainly by K–Ar and partly Rb–Sr and conventional U–Pb methods, yielded ages for most intrusive rocks ranging from 240 to 90 Ma (Shu et al. 1992; Su and Liu 1994). These data, if correct, would imply that the Daye region had a protracted magmatic history lasting from the early Triassic to the late Cretaceous. The plutonic rocks can be broadly grouped as diorites and quartz diorites (Shu et al. 1992), with the latter having an adakite affinity (Wang et al. 2004). Genesis of the adakitic quartz diorites has been interpreted as derivation from melting thickened or delaminated mafic lower crust. The aim of this study was to provide a comprehensive understanding in the age, genesis and geodynamic control of the magmatism of the region. In this contribution, we first present zircon U–Pb ages by sensitive high-resolution ion microprobe (SHRIMP) and laser ablation inductively coupled plasma mass spectrometry (LA-ICP-MS) to precisely date the magmatism. We further use geochemical and Sr–Nd isotope data and results of geochemical modeling to constrain the petrogenesis of the plutonic rocks and show that fractional crystallization of metasomatised mantle-derived magmas has been an important mechanism in generating the adakitic quartz diorites. Finally, we discuss the geodynamic setting that was responsible for the extensive magmatism in light of existing geological, geochronological and geochemical data.

Geological background

The Yangtze craton is separated to the north by the Dabie-Sulu Orogen from the North China craton and to the south by a Neoproterozoic suture from the Cathaysia block (insert of Fig. 1). The eastern part of the craton is confined or cut through by several deep faults, mainly the Xiangfan-Guangji, Yangxin-Changzhou, and Tan-Lu Faults (Fig. 1). Interpretations of geophysical data reveal the existence of the Yangtze River Fault (Fig. 1), which extends for ca. 450 km from Daye in the southwest to Zhenjiang in the northeast (Chang et al. 1991). The eastern Yangtze craton contains seven magmatic regions, which are, from southwest to northeast, the Daye, Jiurui, Anqing, Luzong, Tongling, Ningwu, and Ningzhen (Fig. 1). The Daye region is defined by three major faults, namely the Tan-Lu, Xiangfan-Guangji, and Ma-Tuan Faults (Fig. 2).

The stratigraphy in Daye consists of Ordovician to middle Triassic marine sedimentary rocks (>10,000 m thickness), late Triassic to Cenozoic continental deposits, and Cretaceous volcanic assemblages (Fig. 2). The pre-Triassic strata were intensely folded due to the continental collision between the Yangtze and North China cratons

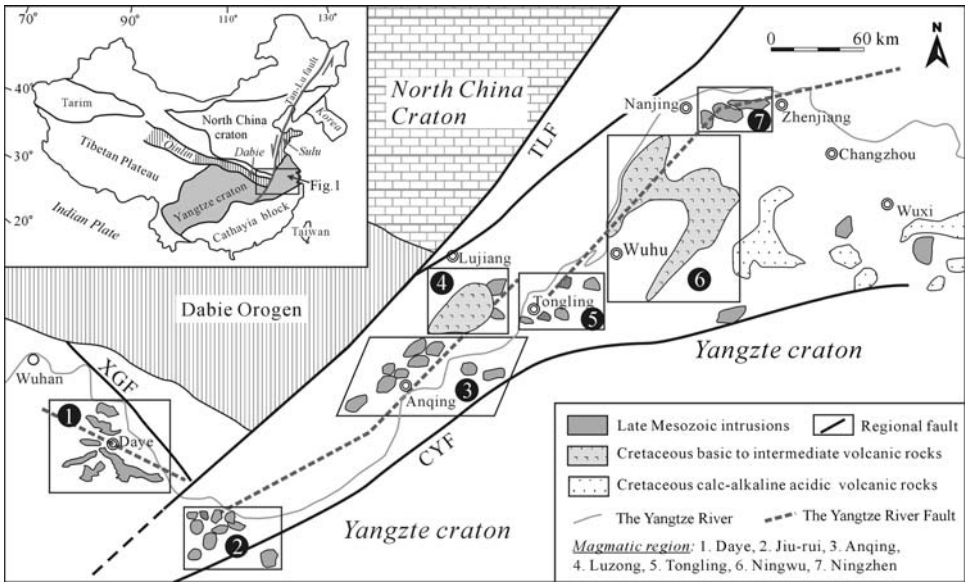

Fig. 1 Schematic illustration of the seven magmatic regions from the eastern Yangtze craton (after Zhai et al. 1992). *TLF* Tan-Lu Fault, *XGF* Xiangfan-Guangji Fault, *CYF* Changzhou-Yangxin Fault

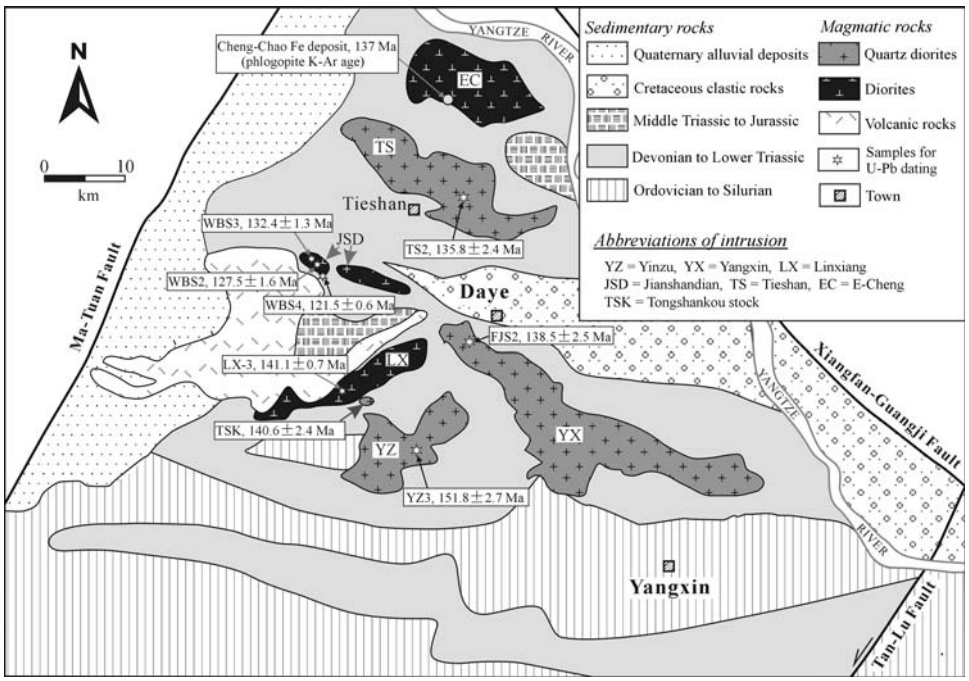

Fig. 2 Geological map of the Daye region (modified from Shu et al. 1992). Also shown are the sampling sites for U–Pb geochronology and the respective ages

during the middle Triassic (Hubei Bureau of Geology, Mineral Resources 1990). Extensive volcanism of the early Cretaceous time resulted in >2,000 m thick volcanic associations, which are grouped, from the base to the top, as the Majiashan, Lingxiang and Dasi Formations (Hubei Bureau of Geology, Mineral Resources 1990). The volcanic rocks have K–Ar ages ranging from 130 to 113 Ma (Shu et al. 1992). Recent SHRIMP zircon U–Pb dating of one dacitic sample from the Dasi Formation yielded a weighted mean $^{206}Pb/^{238}U$ age of 128 ± 1 Ma (Xie et al. 2006). In the SiO_2 versus $K_2O + Na_2O$ diagram, rocks of the Dasi Formation display typical bimodal pattern (Xie et al. 2006).

Several major intrusions were emplaced into the Devonian to early Triassic sedimentary rocks (Fig. 2), including the E'Cheng and Lingxiang diorite, the Jinshandian syenodiorite (hereafter diorite), the Tieshan and Yangxin quartz diorites, and the Yinzu complex consisting of quartz diorite and a small volume of gabbro-diorite. More than 30 granodiorite stocks, mostly less than 1 km^2 of exposure, occur surrounding or intruding the plutons. The Jinshandian diorite consists of the Jinshandian pluton in the east and the Wangbaoshan pluton in the west (Fig. 2). The Tieshan and Lingxiang intrusions contain abundant mafic enclaves composed of variable amounts of plagioclase, hornblende, biotite, pyroxene, and K-feldspar, and accessory titanite, magnetite, and apatite. Monzonite, diorite, and gabbro-diorite dykes, mostly 0.4–2 m wide, intrude the E'cheng, Tieshan, and Jinshandian plutons. The plutons all contain abundant accessory minerals, consisting of zircon, apatite, titanite, and magnetite (Shu et al. 1992).

Analytical methods

U–Pb geochronology

Three samples, each from the Tieshan, Yangxin and Yinzu quartz diorite (Fig. 2) were selected for SHRIMP zircon U–Pb dating. Zircons were handpicked under a binocular microscope after conventional liquid and magnetic separation. About 50–60 grains were mounted in an epoxy resin disc together with chips of the 417-Ma Canberra standard TEMORA (Black et al. 2003). The discs were polished, cleaned, and then gold coated. Prior to isotopic analysis, all grains were photographed under transmitted- and reflected-light, and subsequently examined using the cathodoluminescence (CL) image technique. U–Pb isotopes were analyzed on a SHRIMP II hosted in the Institute of Geology, Chinese Academy of Geological Sciences (Beijing), with procedures similar to Compston et al. (1992). During the SHRIMP analysis, spot size was averaged ca. 30 μm and each spot was rastered over 120 μm for 3 min to remove common Pb on the surface or contamination from the gold coating. The TEMORA zircon standard was used for interelement fractionation correction, and the 572-Ma standard SL13 for determining U, Th, and Pb concentrations. Corrections of common-Pb were applied using the ^{204}Pb-correction method.

Two samples from the Lingxiang and Jinshandian diorites, and the other two from adjacent monzonite and gabbro-diorite dykes (Fig. 2), were collected for LA-ICP-MS zircon U–Pb dating. Analyses were performed on an Elan 6100 DRC ICP-MS, hosted at the Department of

Geology, Northwest University (Xi'an, China). The GeoLas 200 M laser ablation system was used for laser ablation, which is equipped with a 193-nm ArF excimer laser and a homogenizing, imaging optical system. Approximately, 30-μm spot-size was adopted in this study. Helium was used as a carrier gas to enhance transport efficiency of ablated materials. Both standards and samples were arranged on the gas line in order to improve transfer efficiency and reduce elemental fractionation. The $^{207}Pb/^{235}U$ ratio was calculated from the values of $^{207}Pb/^{206}Pb$ and $^{206}Pb/^{238}U$. Common Pb was not subtracted in this work due to the large determination uncertainty of ^{204}Pb, as noted elsewhere (Andersen 2002; Jackson et al. 2004). Analyses of the standard TEMORA 1 as an unknown yielded a weighted $^{206}Pb/^{238}U$ age of 415 ± 4 Ma (MSWD = 0.112, $n = 24$) (Yuan et al. 2004), which is in good agreement with the recommended ID-TIMS age of 416.8 ± 0.2 Ma (Black et al. 2003). Details of analytical procedures have been described in Yuan et al. (2004).

Whole-rock geochemical analysis

Major and trace elemental analysis of 28 fresh whole-rock samples were made at the Department of Earth Science, University of Hong Kong. Samples were crushed and powdered in an agate mill. Major oxides were determined by wavelength-dispersive X-ray fluorescence spectrometry of fused glass beads using a Philips PW2400 spectrometer. Trace elements, including REE, were determined using a VG Plasma-Quad Excel ICP-MS after a 2-day closed beaker digestion using a mixture of HF and HNO_3 acids in high-pressure ''bombs'' (Qi et al. 2000). Pure elemental standard solutions were used for external calibration and BHVO-1 and SY-4 were used as reference materials. The accuracies of the XRFS analyses are estimated at ~2% for elements with concentrations greater than 0.5 wt.% and 5% for those >0.1 wt.%. The uncertainties of the ICP-MS analyses are estimated to be better than ±5% for most trace elements with concentrations >10 ppm, and ±10% for those <10 ppm.

Sr–Nd isotopic determinations

For Rb–Sr and Sm–Nd isotope analyses, 100 mg powder (10–20 μm) of each sample were spiked with mixed isotope tracers (^{87}Rb, ^{84}Sr, ^{149}Sm, ^{150}Nd), and digested in Teflon capsules with a mixture of distilled HF and $HClO_4$ acids. Strontium and REE were separated and purified using cation exchange columns of AG50 W X-12 (200–400 mesh resin). Samarium and Nd were separated and purified using a second exchange column packed with Teflon powder with an exchange medium of HDEHP. Isotopic measurements were conducted on a Finnigan MAT-262 mass spectrometer at the Institute of Geology and Geophysics, Chinese Academy of Sciences (Beijing). Strontium was loaded with a Ta–HF activator on preconditioned Ta filaments and measured in single filament mode. Neodymium was loaded on preconditioned Re filaments and measured in a Re double filament configuration. Mass fractionation corrections for Sr and Nd isotopic ratios were based on values of $^{86}Sr/^{88}Sr = 0.1194$ and $^{146}Nd/^{144}Nd = 0.7219$. Analyses of standard BCR-1 yielded averages of $^{87}Sr/^{86}Sr = 0.704998 \pm 12$ (2σ), $^{143}Nd/^{144}Nd = 0.512658$, $^{147}Sm/^{144}Nd = 0.1411$, Sm = 6.621 ppm, and Nd = 28.40 ppm. Total procedural blanks were <100 pg for Sr and <50 pg for Nd, and the estimated analytical uncertainties of $^{147}Sm/^{144}Nd$ and $^{87}Rb/^{86}Sr$ ratios are <0.5%.

Results

U–Pb geochronology

SHRIMP U–Pb analytical data are summarized in Table 1 and graphically illustrated in the concordia diagrams (Fig. 3). Errors on individual analyses are cited as 1σ, and the weighted mean $^{206}Pb/^{238}U$ ages are quoted at the 95% confidence level.

Sample YZ3 was taken from the Yinzu quartz diorite. Zircons are colorless and generally clear or weakly cloudy, with excellent prism and pyramid faces (Fig. 3a). The crystals range in size from 150 to 300 μm, and their elongation ratios are mostly 2:1 to 3:1. Twelve analyses on ten zircons yielded $^{206}Pb/^{238}U$ ages ranging from 160.9 ± 4.9 to 143.6 ± 6 Ma (Table 1) and constitute a coherent group with a weighted mean $^{206}Pb/^{238}U$ age of 151.8 ± 2.7 Ma (Fig. 3a).

Sample FJS2 was collected from the Yangxin quartz diorite. Zircons are euhedral and 100–200 μm long, with an elongation ratio of 1.5–2:1 (Fig. 3b). Most of them are cloudy and only a few are clear. We analyzed 14 spots on 12 zircons, yielding $^{206}Pb/^{238}U$ ages of 146.8 ± 4.4 to 134.6 ± 4.7 Ma (Table 1). All 14 analyses form a concordant homogeneous group with a weighted mean $^{206}Pb/^{238}U$ age of 138.5 ± 2.5 Ma (Fig. 3b).

Sample TS2 was selected from the Tieshan quartz diorite. Zircons are euhedral, colorless or pale to grey, and generally 200–280 μm long, with an elongation ratio of 1–1.5:1. CL images reveal oscillatory zoning (Fig. 3c). Fourteen analyses were carried out on 11 grains, yielding $^{206}Pb/^{238}U$ ages ranging from 146.3 ± 5 to 127.6 ± 4 Ma (Table 1) and form a coherent group with a weighted mean age of 135.8 ± 2.4 Ma (Fig. 3c).

The LA-ICP-MS zircon analytical results are summarized in Table 2 and illustrated in Fig. 4. Zircons have

Table 1 SHRIMP zircon U–Pb data of the quartz diorite plutons from Daye, eastern China

Spots	U (ppm)	Th (ppm)	$^{232}Th/^{238}U$	$^{206}Pb^*$ (ppm)	$^{206}Pb_c$ (%)	$^{207}Pb^*/^{235}U$	±% (1σ)	$^{207}Pb^*/^{206}Pb^*$	±% (1σ)	$^{206}Pb^*/^{238}U$	±% (1σ)	$^{206}Pb/^{238}U$ Age (Ma)	±1σ
Yinzu diorite, weighted mean age = 151.8 ± 2.8 Ma (MSWD = 1.1)													
YZ3-1	196	105	0.55	4.02	0.47	0.1820	5.7	0.0554	4.7	0.0238	3.1	151.8	4.7
YZ3-2	261	224	0.89	5.29	0.44	0.1500	7.4	0.0463	6.7	0.0235	3.1	149.4	4.5
YZ3-3	168	121	0.75	3.27	0.88	0.1620	8.9	0.0521	7.8	0.0225	4.3	143.6	6.0
YZ3-4	238	172	0.75	4.85	0.44	0.1742	5.5	0.0536	4.6	0.0236	3.1	150.3	4.5
YZ3-5	182	96	0.55	3.91	1.46	0.1430	13	0.0421	12	0.0246	3.1	156.9	4.9
YZ3-6	270	192	0.73	5.69	0.68	0.1556	5.1	0.0463	4.1	0.0244	3.1	155.2	4.7
YZ3-7	191	107	0.58	3.91	0.91	0.1590	9.6	0.0486	9.1	0.0237	3.1	150.8	4.6
YZ3-8	275	173	0.65	5.89	0.45	0.1600	6.8	0.0468	6	0.0248	3.1	157.9	4.8
YZ3-9	279	200	0.74	5.65	0.53	0.1650	6.4	0.0510	5.6	0.0234	3.1	149.2	4.5
YZ3-10	207	135	0.68	4.08	0.65	0.1602	5.5	0.0509	4.6	0.0229	3.1	145.7	4.5
YZ3-11	391	207	0.55	8.53	0.51	0.1614	5.7	0.0463	4.8	0.0253	3.0	160.9	4.8
YZ3-12	212	152	0.74	4.28	0.50	0.1643	5.6	0.0509	4.7	0.0234	3.1	149.0	4.5
Yangxin quartz diorite, weighted mean age = 138.5 ± 2.5 Ma (MSWD = 0.8)													
FJS2-1	77	79	1.06	1.46	3.76	0.0970	21	0.0332	21	0.0211	3.5	134.6	4.7
FJS2-2	117	124	1.09	2.24	1.16	0.1560	11	0.0514	10	0.0220	3.3	140.3	4.6
FJS2-3	93	58	0.64	1.71	0.68	0.1730	9.3	0.0591	8.7	0.0213	3.5	135.6	4.7
FJS2-4	124	103	0.86	2.3	0.00	0.1802	5.5	0.0607	4.4	0.0215	3.3	137.3	4.5
FJS2-5	92	83	0.94	1.81	0.00	0.1890	10	0.0600	9.3	0.0229	3.7	145.9	5.3
FJS2-6	161	148	0.95	2.97	1.30	0.0590	29	0.0203	29	0.0212	3.3	135.5	4.4
FJS2-7	222	269	1.25	4.1	0.57	0.1400	6.2	0.0475	5.3	0.0214	3.2	136.2	4.3
FJS2-8	138	138	1.03	2.61	0.00	0.1707	5.5	0.0564	4.4	0.0220	3.2	140.0	4.4
FJS2-9	212	183	0.89	3.96	0.93	0.1360	11	0.0457	9.5	0.0216	5.3	137.5	7.2
FJS2-10	299	271	0.94	5.94	0.57	0.1563	6.1	0.0492	5.2	0.0230	3.0	146.8	4.4
FJS2-11	151	179	1.22	2.81	2.25	0.1160	17	0.0396	16	0.0212	3.3	135.2	4.4
FJS2-12	105	89	0.87	1.94	0.00	0.1670	7.2	0.0564	6.4	0.0215	3.3	137.1	4.4
FJS2-13	151	140	0.96	2.77	1.08	0.1480	11	0.0505	11	0.0212	3.2	135.2	4.3
FJS2-14	133	169	1.31	2.61	1.25	0.1360	14	0.0436	13	0.0226	3.2	143.9	4.6
Tieshan diorite, weighted mean age = 135.8 ± 2.4 Ma (MSWD = 1.4)													
TS2-1	363	949	2.70	6.27	0.73	0.1267	7.5	0.0460	6.8	0.0200	3.2	127.6	4.0
TS2-2	163	233	1.47	2.94	0.80	0.1430	8.5	0.0498	7.8	0.0208	3.3	132.7	4.3
TS2-3	119	174	1.51	2.22	0.83	0.1550	10	0.0520	9.7	0.0216	3.3	137.5	4.5
TS2-4	102	130	1.31	2.01	0.00	0.1770	6.2	0.0560	5.2	0.0230	3.4	146.3	5.0
TS2-5	215	291	1.40	3.95	0.00	0.1488	5.1	0.0505	4	0.0214	3.2	136.3	4.3
TS2-6	114	126	1.14	2.13	1.12	0.1610	17	0.0541	17	0.0215	3.4	137.3	4.7
TS2-7	99	113	1.17	1.88	1.69	0.1410	13	0.0469	12	0.0218	3.4	138.8	4.6
TS2-8	96	132	1.42	1.9	1.90	0.1630	14	0.0523	14	0.0225	3.5	143.7	4.9
TS2-9	57	52	0.93	1.04	3.17	0.1160	38	0.0410	38	0.0204	4.1	130.0	5.3
TS2-10	176	217	1.27	3.34	0.67	0.1570	10	0.0519	9.9	0.0220	3.2	140.1	4.5
TS2-11	358	535	1.54	6.35	0.86	0.1220	8.2	0.0432	7.6	0.0205	3.1	130.7	4.0
TS2-12	257	472	1.89	4.52	0.34	0.1530	6.9	0.0544	6.1	0.0204	3.3	130.1	4.2
TS2-13	110	130	1.22	2.08	1.16	0.1590	12	0.0528	11	0.0218	3.4	139.0	4.6
TS2-14	102	131	1.33	1.93	1.77	0.1440	15	0.0483	14	0.0217	3.4	138.1	4.7

[a] Pb^* and Pb_c indicate radiogenic and non-radiogenic Pb

[b] Common Pb corrected using measured ^{204}Pb

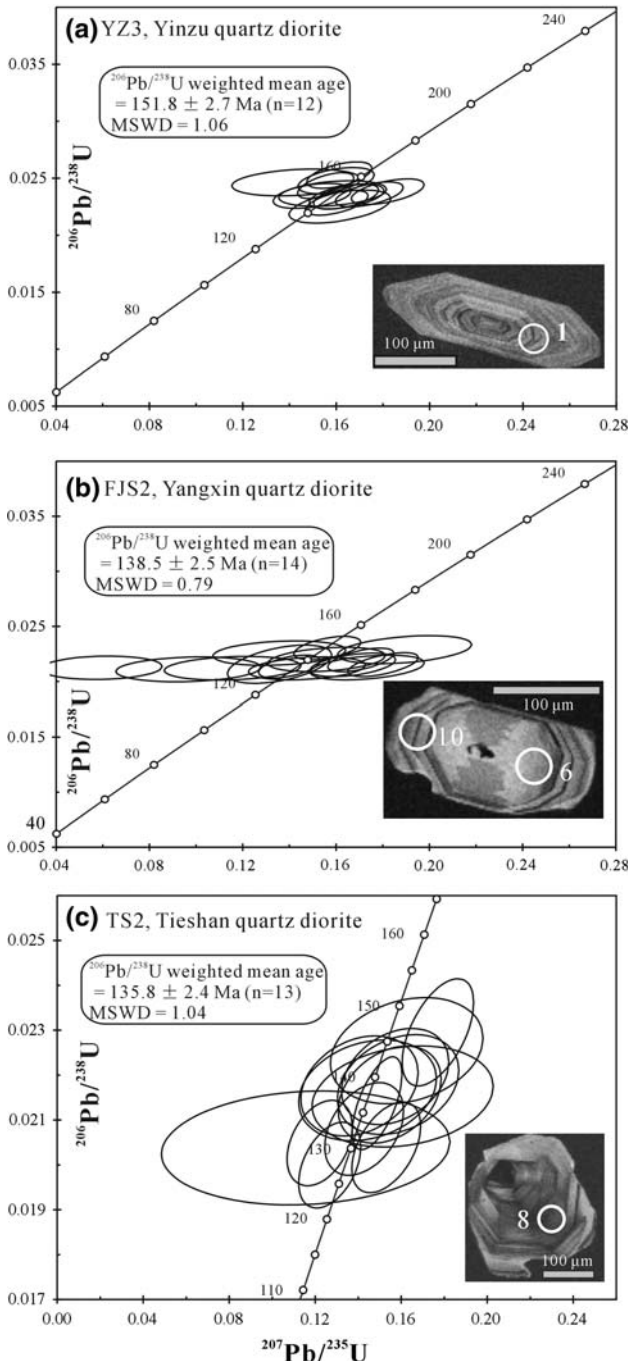

Fig. 3 SHRIMP U–Pb concordia diagrams for the Yinzu (**a**), Yangxin (**b**), and Tieshan (**c**) quartz diorites

oscillatory zoning typical of magmatic origin, similar in morphology and texture to those used for SHRIMP analysis. Sample LX3 was selected from the Lingxiang diorite. Nineteen analyses of 20 yielded ^{206}Pb/^{238}U ages ranging from 143 ± 1 to 138 ± 1 Ma, forming a coherent group that gave a weighted mean ^{206}Pb/^{238}U age of 141.1 ± 0.7 Ma (Fig. 4a). The remaining one has a slightly younger age of 136.6 ± 0.9 Ma (LX3-F.09; Table 2).

Sample WBS3 was taken from the Wangbaoshan pluton of the Jinshandian diorite (Fig. 2). Twenty analyses on 18 zircon crystals yielded ages that cluster in two groups (Fig. 4b). The first group comprises 14 analyses ranging in age from 136 ± 2 to 128 ± 2 Ma, with a weighted mean ^{206}Pb/^{238}U age of 132.4 ± 1.3 Ma that is interpreted as the crystallization age for the Jinshandian diorite. The second group comprises six analyses, whose ages are 124 ± 1 to 121 ± 1 Ma. The younger ages resulted possibly from analytical uncertainties due to signal instability.

Sample WBS2 was collected from a 1.5-m-wide, NE-striking fine-grained monzonite dyke that intruded the Wangbaoshan pluton. Nineteen analyses were carried out on 18 zircon grains. One analysis yielded an old age of 141 ± 2 Ma that is identical to the age of sample LX3 (Fig. 4a) and thus interpreted as an inheritance from the nearby Lingxiang diorite or contamination by the sample LX3 during sample preparation. The remaining 18 analyses form two coherent groups that have weighted mean ^{206}Pb/^{238}U age of 127.5 ± 1.6 Ma (n = 14) and 118.9 ± 2.2 Ma (n = 4), respectively (Fig. 4c). The weighted mean age of the first group is interpreted as the crystallization age of the dyke, whereas the second group may have resulted from signal instability during analysis.

Sample WBS4 was selected from a 1.2-m-wide gabbro-diorite dyke emplaced into the late Jurassic conglomerate, 200 m southeast of the Wangbaoshan pluton (Fig. 2). Twenty analyses from 19 zircons yielded ages ranging from 125 ± 2 to 119 ± 2 Ma (Table 2). The weighted mean ^{206}Pb/^{238}U age of 121.5 ± 0.6 Ma (Fig. 4d) is interpreted as the crystallization age for the gabbro-diorite dyke.

Whole-rock geochemistry

Major and trace elemental contents are listed in Table 3 and illustrated in Figs. 5, 6 and 7. The rocks have silica between 52.3 and 69.9 wt.% and total alkali of 4–9.6 wt.% and can be broadly grouped as diorite (Lingxiang and Jinshandian plutons) and quartz diorite (Yangxin, Tieshan, and Yinzu plutons) (Fig. 5a). Most samples plot in the high-K field in the SiO_2 versus K_2O diagram (Fig. 5b). They have A/CNK ratio [molar $Al_2O_3/(CaO + Na_2O + K_2O)$] mostly between 0.73 and 0.96 (Table 3) and A/NK ratio [molar $Al_2O_3/(Na_2O + K_2O)$] of 1.3–2.3, indicating a metaluminous affinity (Fig. 5c), consistent with the presence of normative diopside in most samples (Table 3). The Na_2O/K_2O ratios of 1.3–3 (except samples YZ2 and JS1) indicate the rocks are sodic (Table 3), as demonstrated by the K–Na–Ca cationic ternary plot in which they follow a TTG differentiation rather than a calc-alkaline trend (Fig. 5d). Rocks have MgO and Mg$^{\#}$ [100 × molar Mg/(Mg + Fe) ratio] of 0.64–3.46 wt.% and 21–48, respectively. Samples JS1, TS3 and YZ2 are somehow different

Table 2 LA-ICPMS zircon U–Pb data of diorite plutons and dykes from Daye, eastern China

Spot	Isotope ratios						Age (Ma)			
	$^{207}Pb/^{206}Pb$	$\pm1\sigma$	$^{207}Pb/^{235}U$	$\pm1\sigma$	$^{206}Pb/^{238}U$	$\pm1\sigma$	$^{207}Pb/^{235}U$	$\pm1\sigma$	$^{206}Pb/^{238}U$	$\pm1\sigma$
Lingxiang diorite, weighted mean $^{206}Pb/^{238}U$ age = 141.1 ± 0.7 Ma										
LX3-F.01	0.0507	0.0016	0.1556	0.0046	0.0222	0.0002	147	4	142	1
LX3-F.02	0.0502	0.0012	0.1555	0.0035	0.0225	0.0002	147	3	143	1
LX3-F.03	0.0510	0.0013	0.1535	0.0035	0.0219	0.0002	145	3	139.3	0.9
LX3-F.04	0.0523	0.0014	0.1600	0.0042	0.0222	0.0001	151	4	141.6	0.9
LX3-F.05	0.0489	0.0020	0.1488	0.0059	0.0221	0.0002	141	5	141	1
LX3-F.06	0.0492	0.0015	0.1490	0.0045	0.0220	0.0002	141	4	140.2	1
LX3-F.07	0.0519	0.0013	0.1596	0.0036	0.0223	0.0002	150	3	142.2	0.9
LX3-F.08	0.0497	0.0022	0.1508	0.0065	0.0220	0.0002	143	6	140	1
LX3-F.09	0.0486	0.0013	0.1436	0.0034	0.0214	0.0002	136	3	136.6	0.9
LX3-F.10	0.0521	0.0008	0.1604	0.0021	0.0223	0.0001	151	2	142.3	0.8
LX3-F.11	0.0510	0.0015	0.1577	0.0044	0.0224	0.0002	149	4	143	1
LX3-F.12	0.0501	0.0013	0.1536	0.0037	0.0222	0.0002	145	3	142	1
LX3-F.13	0.0535	0.0019	0.1636	0.0056	0.0222	0.0002	154	5	141	1
LX3-F.14	0.0463	0.0028	0.1394	0.0083	0.0218	0.0002	132	7	139	1
LX3-F.15	0.0525	0.0023	0.1604	0.0066	0.0222	0.0002	151	6	141	1
LX3-F.16	0.0469	0.0023	0.1409	0.0068	0.0218	0.0002	134	6	139	1
LX3-F.17	0.0488	0.0014	0.1498	0.0039	0.0223	0.0002	142	3	142	1
LX3-F.18	0.0512	0.0013	0.1565	0.0037	0.0222	0.0002	148	3	141	1
LX3-F.19	0.0547	0.0020	0.1691	0.0057	0.0224	0.0002	159	5	143	1
LX3-F.20	0.0536	0.0024	0.1593	0.0069	0.0216	0.0002	150	6	138	1
Jinshandian diorite										
Group 1, weighted mean $^{206}Pb/^{238}U$ age = 132.4 ± 1.3 Ma (n = 14)										
WBS3-01	0.0485	0.0024	0.1411	0.0067	0.0212	0.0002	134	6	135	2
WBS3-02	0.0624	0.0042	0.1730	0.0115	0.0201	0.0003	162	10	128	2
WBS3-03	0.0754	0.0023	0.2171	0.0063	0.0209	0.0002	200	5	134	1
WBS3-04	0.0667	0.0032	0.1925	0.0089	0.0210	0.0003	179	8	134	2
WBS3-05	0.0542	0.0012	0.1512	0.0031	0.0203	0.0002	143	3	130	1
WBS3-06	0.0412	0.0021	0.1178	0.0059	0.0208	0.0002	113	5	132	2
WBS3-10	0.0477	0.0022	0.1367	0.0061	0.0208	0.0002	130	5	133	1
WBS3-11	0.0562	0.0038	0.1600	0.0106	0.0207	0.0003	151	9	132	2
WBS3-12	0.0490	0.0041	0.1407	0.0115	0.0208	0.0004	134	10	133	2
WBS3-13	0.0535	0.0028	0.1546	0.0079	0.0210	0.0003	146	7	134	2
WBS3-16	0.0736	0.0048	0.2074	0.0130	0.0204	0.0003	191	11	130	2
WBS3-17	0.0555	0.0030	0.1625	0.0086	0.0213	0.0003	153	8	136	2
WBS3-18	0.0537	0.0041	0.1573	0.0116	0.0213	0.0003	148	10	136	2
WBS3-20	0.0542	0.0034	0.1544	0.0094	0.0207	0.0003	146	8	132	2
Group 2, weighted mean $^{206}Pb/^{238}U$ age = 122.9 ± 1.5 Ma (n = 6)										
WBS-3.06	0.0468	0.0023	0.1248	0.0059	0.0194	0.0002	119	5	124	1
WBS-3.08	0.0656	0.0020	0.1712	0.0049	0.0190	0.0002	160	4	121	1
WBS-3.09	0.0610	0.0020	0.1629	0.0052	0.0194	0.0002	153	5	124	1
WBS-3.14	0.0471	0.0040	0.1234	0.0102	0.0190	0.0004	118	9	122	2
WBS-3.15	0.0560	0.0036	0.1481	0.0091	0.0192	0.0003	140	8	123	2
WBS-3.19	0.0478	0.0056	0.1266	0.0145	0.0192	0.0004	121	13	123	3

Table 2 continued

Spot	Isotope ratios						Age (Ma)			
	$^{207}Pb/^{206}Pb$	$\pm1\sigma$	$^{207}Pb/^{235}U$	$\pm1\sigma$	$^{206}Pb/^{238}U$	$\pm1\sigma$	$^{207}Pb/^{235}U$	$\pm1\sigma$	$^{206}Pb/^{238}U$	$\pm1\sigma$
Wangbaoshan monzonite dyke										
Group 1, weighted mean $^{206}Pb/^{238}U$ age = 127.5 ± 1.6 Ma (n = 14)										
WBS2-03	0.0835	0.0027	0.2366	0.0073	0.0206	0.0002	216	6	131	1
WBS2-04	0.0504	0.0019	0.1359	0.0050	0.0196	0.0001	129	4	125	1
WBS2-06	0.0487	0.0024	0.1335	0.0065	0.0199	0.0002	127	6	127	1
WBS2-08	0.0492	0.0019	0.1367	0.0050	0.0202	0.0002	130	4	129	1
WBS2-09	0.0492	0.0034	0.1338	0.0090	0.0197	0.0002	128	8	126	1
WBS2-10	0.0549	0.0030	0.1571	0.0083	0.0208	0.0002	148	7	132	1
WBS2-11	0.0500	0.0036	0.1376	0.0097	0.0200	0.0002	131	9	127	1
WBS2-12	0.0500	0.0034	0.1349	0.0091	0.0196	0.0002	129	8	125	1
WBS2-13	0.0546	0.0037	0.1506	0.0101	0.0200	0.0002	142	9	128	2
WBS2-16	0.0491	0.0025	0.1306	0.0064	0.0193	0.0002	125	6	123	1
WBS2-17	0.0508	0.0023	0.1387	0.0061	0.0198	0.0002	132	5	126	1
WBS2-18	0.0503	0.0028	0.1399	0.0075	0.0202	0.0002	133	7	129	1
WBS2-19	0.0500	0.0024	0.1352	0.0064	0.0196	0.0002	129	6	125	1
WBS2-20	0.0473	0.0009	0.1338	0.0024	0.0205	0.0001	128	2	131	1
Group 2, weighted mean $^{206}Pb/^{238}U$ age = 118.9 ± 2.2 Ma (n = 4)										
WBS2-01	0.0536	0.0044	0.1372	0.0112	0.0186	0.0002	131	10	119	1
WBS2-06	0.0492	0.0022	0.1258	0.0054	0.0185	0.0002	120	5	118.4	0.9
WBS2-13	0.0480	0.0032	0.1213	0.0080	0.0183	0.0002	116	7	117	1
WBS2-14	0.0521	0.0022	0.1354	0.0057	0.0188	0.0001	129	5	120.3	0.8
Wangbaoshan diorite porphyry dyke, weighted mean $^{206}Pb/^{238}U$ age = 121.5 ± 0.6 Ma										
WBS4-01	0.0507	0.0029	0.1318	0.0073	0.0189	0.0003	126	7	120	2
WBS4-02	0.0500	0.0018	0.1296	0.0046	0.0188	0.0002	124	4	120	1
WBS4-03	0.0558	0.0022	0.1463	0.0054	0.0190	0.0002	139	5	121	1
WBS4-04	0.0431	0.0031	0.1142	0.0080	0.0192	0.0002	110	7	123	1
WBS4-05	0.0484	0.0013	0.1273	0.0032	0.0191	0.0001	122	3	122	1
WBS4-06	0.0502	0.0032	0.1307	0.0080	0.0189	0.0003	125	7	121	2
WBS4-07	0.0541	0.0062	0.1401	0.0159	0.0188	0.0004	133	14	120	2
WBS4-08	0.0523	0.0025	0.1372	0.0063	0.0190	0.0002	131	6	122	1
WBS4-09	0.0492	0.0038	0.1295	0.0097	0.0191	0.0003	124	9	122	2
WBS4-10	0.0543	0.0034	0.1433	0.0089	0.0191	0.0003	136	8	122	2
WBS4-11	0.0540	0.0025	0.1414	0.0062	0.0190	0.0002	134	6	121	1
WBS4-12	0.0475	0.0033	0.1259	0.0087	0.0192	0.0003	120	8	123	2
WBS4-13	0.0530	0.0047	0.1361	0.0118	0.0186	0.0004	130	11	119	2
WBS4-14	0.0489	0.0024	0.1289	0.0061	0.0191	0.0002	123	5	122	1
WBS4-15	0.0514	0.0028	0.1353	0.0071	0.0191	0.0002	129	6	122	1
WBS4-16	0.0555	0.0044	0.1437	0.0111	0.0188	0.0003	136	10	120	2
WBS4-17	0.0503	0.0028	0.1321	0.0071	0.0190	0.0002	126	6	122	1
WBS4-18	0.0461	0.0035	0.1195	0.0089	0.0188	0.0002	115	8	120	2
WBS4-19	0.0514	0.0034	0.1387	0.0089	0.0196	0.0003	132	8	125	2
WBS4-20	0.0499	0.0032	0.1303	0.0082	0.0190	0.0003	124	7	121	2

from others of the same pluton (Fig. 5). Both diorites and quartz diorites have high Al_2O_3 (15.1–19.3 wt.%), Na_2O (3.0–7.2 wt.%), Sr (634–2087 ppm), but low Rb (27–119 ppm), Ni (5–28 ppm), Cr (10–34 ppm), Nb (7–26 ppm) and Zr (42–166 ppm). The quartz diorite samples show an adakite geochemical affinity, marked by

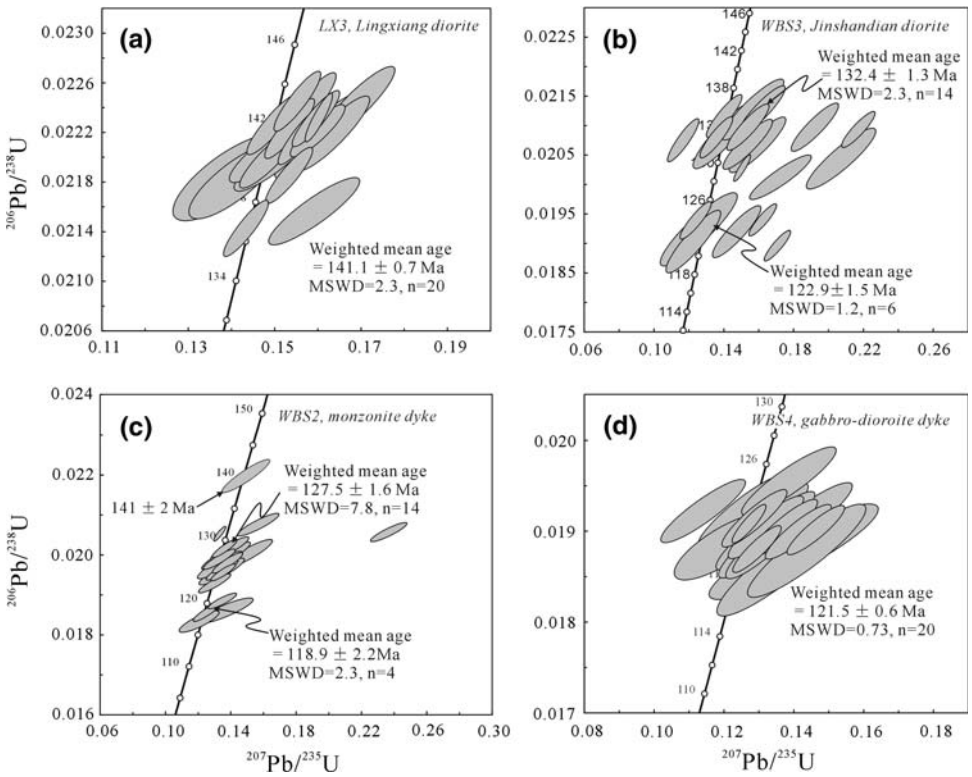

Fig. 4 Concordia diagrams of LA-ICP-MS zircon U–Pb data for the Lingxiang (**a**) and Jinshandian diorites (**b**), and late-stage dykes (**c**, **d**)

low Y (7–22 ppm), Yb (0.5–1.8 ppm), and Sc (5–15 ppm) and high Sr/Y (46–128) and La/Yb (32–63) ratios.

Figure 6 illustrates the Harker diagrams of selected major and trace elements taking SiO_2 as differentiation index. With exceptions of samples TS3, JS1 and YZ2, the rocks show a linear or curvilinear trend in most Harker diagrams, suggesting close petrogenetic relationships between the diorites and quartz diorites. Major oxides including Al_2O_3, FeO^T, MgO, CaO, TiO_2 and $P2O_5$ and trace elements such as Sc, Yb, V, and Y decrease with increasing SiO_2, indicating fractionation of hornblende, plagioclase, apatite, and Fe–Ti oxides.

Both diorite and quartz diorite exhibit similar, subparallel chondrite-normalized REE patterns, characterized by strong fractionation between LREE and HREE, without significant Eu anomalies (Fig. 7a, b). The quartz diorites are more HREE depleted than the diorites, marked by $(La/Yb)_N$ values of 21–43 and 9–22 and Yb_N of 3–11 and 9–15, respectively (Table 3; Fig. 7a, b). In the primitive mantle-normalized spiderdiagram (Fig. 7c, d), both quartz diorites and diorites are enriched in highly incompatible elements such as LREE and large ion lithophile elements (LILE), but depleted in high field strength elements (HFSE), with prominent negative anomalies of Ta–Nb and Ti. The quartz diorites are more so than the diorites, with $(Rb/Lu)_N$ ratios of 67–80 and 36–50, respectively (not shown).

Sr–Nd isotope data

The Rb–Sr and Sr–Nd isotope data are reported in Table 4 and Fig. 8. Data of the 141-Ma Tongshankou granodiorite (Li et al. 2008) and the 128-Ma basalts of the Dasi Formation (Xie et al. 2006) from the same region are also included for comparison. Initial $^{87}Sr/^{86}Sr$ and $^{143}Nd/^{144}Nd$ ratios were calculated using the crystallization age of each intrusion. In the $\varepsilon_{Nd}(t)$ versus $(^{87}Sr/^{86}Sr)_t$ diagram (Fig. 8), both quartz diorites and diorites lie in the enriched extension of the mantle array defined by mantle-derived rocks. The samples have similar, radiogenic, relatively homogeneous Sr–Nd isotopic compositions, characterized by $(^{87}Sr/^{86}Sr)_t = 0.7058–0.7091$, $(^{143}Nd/^{144}Nd)_t = 0.512019–0.512294$, and $\varepsilon_{Nd}(t) = -3.4$ to -8.8. These values are strikingly distinct from the lower crust of the Yangtze and North China cratons (Ames et al. 1996; Jahn et al. 1999) and the young upper continental crust (Taylor and McLennan 1985) as well. They also differ significantly from the Archean Kongling orthogneiss of the Yangtze craton (Ames et al. 1996). Instead, the Sr–Nd isotope data overlap those of the early Cretaceous basalts or their plutonic equivalents from Daye (Xie et al. 2006), Luzong (Liu et al. 2002; Wang et al. 2006), Ningwu (Wang et al. 2001), and Tongling regions (Yan et al. 2008) of the eastern Yangtze craton (Fig. 1), which have been demonstrated to have an enriched-mantle affinity.

Table 3 Major and trace elemental abundances of plutonic rocks from Daye, eastern China

Pluton Sample	Lingxiang					Jinshandian				Yinzu					Tieshan				
	LX1	LX2	LX3	LX4	LX5	JS1	JS2	JS3	JS4	YZ1	YZ2	YZ3	YZ4	YZ5	TS1	TS2	TS3	TS4	00HB1
Major oxides (wt.%)																			
SiO_2	57.23	57.38	55.46	52.31	57.81	54.93	55.44	54.28	56.45	64.88	69.91	65.85	65.02	66.50	63.51	62.93	60.24	63.49	63.77
TiO_2	0.87	0.84	0.91	0.87	0.86	1.06	1.00	1.06	0.98	0.39	0.39	0.36	0.46	0.45	0.55	0.58	0.65	0.53	0.62
$A_{l2}O_3$	17.03	17.13	17.57	17.90	16.89	16.93	17.18	17.52	17.48	15.68	12.42	15.90	15.00	15.05	15.92	15.85	19.31	16.39	15.81
FeO^t	6.85	6.66	7.41	8.22	6.74	3.36	7.12	7.16	6.56	3.26	2.92	2.99	3.44	3.02	3.88	3.74	3.42	4.33	3.90
MnO	0.14	0.14	0.16	0.15	0.14	0.16	0.11	0.09	0.10	0.06	0.13	0.06	0.10	0.08	0.06	0.06	0.02	0.09	0.06
MgO	2.76	2.69	2.96	3.46	2.67	2.57	2.28	2.29	2.23	1.46	1.32	1.30	1.43	1.55	1.20	1.48	0.64	1.59	1.62
CaO	6.79	6.70	7.43	8.43	6.77	10.27	6.15	7.02	5.99	3.75	5.75	3.37	4.81	4.22	4.00	4.37	2.70	4.39	3.99
Na_2O	3.16	3.35	3.27	3.48	3.04	3.62	4.57	4.25	4.65	4.15	3.72	4.29	4.08	4.22	5.14	5.32	7.18	4.31	4.84
K_2O	2.44	2.51	2.05	1.83	2.49	4.12	2.83	2.64	2.83	3.13	0.29	3.04	2.72	2.21	2.94	3.01	2.41	2.82	3.30
P_2O_5	0.33	0.35	0.39	0.43	0.33	0.51	0.46	0.47	0.45	0.18	0.18	0.14	0.23	0.19	0.22	0.23	0.20	0.25	0.24
LOI	1.32	1.33	1.27	1.84	1.34	0.85	1.07	1.00	1.32	2.02	1.64	1.44	1.21	1.37	1.10	0.71	1.47	0.64	1.32
Total	98.92	99.08	98.88	98.92	99.08	98.38	98.21	97.78	99.04	98.96	98.67	98.74	98.50	98.86	98.52	98.28	98.24	98.83	99.47
Mg#	41.8	41.8	41.6	42.8	41.4	57.7	36.3	36.3	37.7	44.4	44.6	43.6	42.5	47.8	35.5	41.3	25.0	39.5	42.5
Na_2O/K_2O	1.30	1.33	1.60	1.90	1.22	0.88	1.61	1.61	1.64	1.33	12.83	1.41	1.50	1.91	1.75	1.77	2.98	1.53	1.47
$Na_2O + K_2O$	5.60	5.86	5.32	5.31	5.53	7.74	7.40	6.89	7.48	7.28	4.01	7.33	6.8	6.43	8.08	8.33	9.59	7.13	8.14
A/CNK	0.84	0.84	0.83	0.78	0.84	0.58	0.79	0.77	0.81	0.92	0.73	0.96	0.81	0.88	0.84	0.79	1.00	0.90	1.04
Trace elements (ppm)																			
Ba	874	885	853	790	581	1,223	816	710	688	1,332	800	1,404	1,227	906	1,320	1,164	1,360	904	1,016
Cr	24	34	27	24	17	10	26	31	24	21	12	21	23	19	26	31	24	20	26
Hf	2.30	2.63	2.48	2.67	2.44	3.58	2.74	1.87	1.92	2.78	1.26	2.33	1.43	1.75	1.47	1.65	1.6	1.1	5.07
Nb	7	9	8	9	7	21	26	18	21	17	15	17	15	14	17	15	7	20	13
Ni	21	22	27	22	23	17	26	28	24	13	16	15	12	12	26	28	24	21	14
Rb	76	79	75	63	51	103	80	63	68	85	14	90	111	71	75	76	27	87	85
Sc	16.9	15.9	14.7	18	19.4	13.7	23.1	11.5	18.9	13.9	5.7	6.7	8.9	12.9	9.0	18.3	5.5	8.2	5
Sr	667	634	649	652	749	1,440	1,185	1,041	1,145	1,157	1,140	1,382	988	978	2,087	1,440	1,407	1,059	1,609
Ta	0.51	0.63	0.58	0.63	0.41	1.19	0.92	0.69	0.92	0.72	0.61	0.67	0.65	0.67	0.74	0.77	0.36	0.92	0.75
Th	6.1	6.9	8.5	7.6	5.1	8.1	10	7.5	9.4	14.8	9	14	12.2	13.1	6.8	8.7	2.3	11.0	7.5
U	1.45	1.81	1.68	1.81	1.1	1.96	1.65	1.36	1.42	2.98	2.64	3	3.71	2.91	1.40	2.4	0.4	1.6	2.24
V	167	161	147	172	137	145	171	159	144	60	39	60	73	61	83	86	66	79	69
Y	17	18	17	22	23	28	29	23	25	15	10	14	13	13	16	15	7	17	13
Zr	80	93	84	88	81	122	136	66	54	121	42	114	53	65	53	54	49	37	166
La	28.71	30.8	31.70	32.89	28.44	58.9	60.29	58.30	62.16	48.11	29	44.66	37.7	42.93	44.71	42.99	32.3	44.6	42.58
Ce	55.19	59.85	59.16	66.24	60.28	124.28	119.25	110.51	123.72	91.87	60.41	86.38	74.54	83.37	89.63	87.91	61	87	84.78
Pr	6.35	7.11	6.76	7.97	7.75	15.68	14.83	13.12	14.92	10.93	7.59	10.15	9.04	9.95	11.1	10.97	7.7	10.4	9.32
Nd	25.02	27.09	25.14	31.54	31.76	63.47	57.57	48.54	54.23	36.97	25.18	35.13	32.01	34.73	41.83	40.72	26	36	35.44
Sm	4.96	5.37	4.82	6.19	6.51	11.43	9.39	8.59	9.52	5.7	4.3	5.29	5	5.42	7.06	6.92	4.74	6.18	6.41
Eu	1.45	1.49	1.51	1.64	1.8	2.9	2.38	2.31	2.46	1.5	1.1	1.38	1.28	1.36	1.76	1.76	1.83	1.6	1.73

Table 3 continued

Pluton Sample	Lingxiang					Jinshandian				Yinzu					Tieshan				
	LX1	LX2	LX3	LX4	LX5	JS1	JS2	JS3	JS4	YZ1	YZ2	YZ3	YZ4	YZ5	TS1	TS2	TS3	TS4	00HB1
Gd	4.21	4.45	4.08	5.24	5.46	10.35	7.17	7.46	7.48	4.54	2.81	4.69	4.6	4.17	5.89	5.36	3.71	5.29	4.4
Tb	0.59	0.64	0.58	0.74	0.8	1.07	0.87	0.82	0.87	0.46	0.34	0.42	0.42	0.44	0.61	0.56	0.35	0.54	0.55
Dy	3.19	3.42	3.12	4.1	4.45	5.28	4.31	4.12	4.38	2.25	1.71	1.96	2.02	2.17	2.9	2.69	1.61	2.63	2.85
Ho	0.63	0.66	0.62	0.8	0.86	1.09	0.87	0.85	0.89	0.45	0.34	0.39	0.4	0.43	0.59	0.53	0.29	0.54	0.49
Er	1.73	1.92	1.74	2.22	2.49	2.78	2.23	2.15	2.26	1.18	0.9	1.02	1.06	1.17	1.47	1.34	0.7	1.41	1.29
Tm	0.24	0.26	0.24	0.32	0.33	0.39	0.31	0.31	0.31	0.17	0.13	0.15	0.15	0.17	0.2	0.18	0.09	0.2	0.18
Yb	1.54	1.73	1.6	1.99	2.14	2.42	1.87	1.88	1.94	1.1	0.79	0.93	0.95	1.01	1.22	1.09	0.51	1.29	1.09
Lu	0.23	0.24	0.24	0.29	0.3	0.34	0.26	0.29	0.27	0.16	0.11	0.13	0.14	0.15	0.17	0.15	0.07	0.18	0.15
Sr/Y	40.1	35.2	38.7	30.2	32.4	50.7	40.7	44.4	45.9	78.1	112.4	98.1	75.4	75.3	127.6	99.1	202.1	64.2	121.3
$(La/Yb)_N$	12.6	12	13.4	11.2	9	16.4	21.8	20.9	21.6	29.5	24.8	32.4	26.8	28.7	24.7	26.6	42.8	23.3	26.4
Yb_N	9.3	10.5	9.7	12.1	13	14.7	11.3	11.4	11.8	6.7	4.8	5.6	5.8	6.1	7.4	6.6	3.1	7.8	6.6
Diopside	5.5	3.2	6.1	9.6	5.4	20.5	8.2	9.3	7.1	2.2	9.3	0.5	9.3	3.4	5.7	8.2		2.7	
Nepheline						1.6													
Corundum																	0.5		2

Pluton sample	Yangxin									
	YX1	YX2	YX3	YX4	YX5	YX6	YX7	YX8	YX9	YX10
Major oxides (wt.%)										
SiO_2	59.70	61.46	59.82	63.19	62.06	59.93	62.04	60.67	61.90	60.71
TiO_2	0.59	0.54	0.62	0.54	0.60	0.58	0.56	0.69	0.62	0.64
$A_{l2}O_3$	17.18	16.38	16.91	16.16	16.65	17.49	17.06	16.34	16.32	16.58
FeO^t	4.96	4.24	3.91	4.20	4.55	4.88	4.46	5.47	4.87	5.12
MnO	0.07	0.05	0.09	0.08	0.07	0.08	0.03	0.12	0.10	0.10
MgO	0.92	1.89	0.97	1.43	1.40	1.16	0.68	1.96	1.68	1.96
CaO	5.10	4.79	6.54	4.48	5.29	5.32	3.73	5.17	4.67	4.78
Na_2O	4.49	4.42	4.36	4.42	4.36	4.62	4.11	4.82	4.63	4.63
K_2O	2.58	3.31	2.77	2.87	2.74	2.62	3.13	2.23	3.09	3.23
P_2O_5	0.25	0.26	0.32	0.24	0.28	0.27	0.26	0.30	0.26	0.28
LOI	2.31	1.64	2.94	1.10	1.32	1.85	2.80	0.84	0.84	0.69
Total	98.15	98.98	99.25	98.71	99.32	98.80	98.86	98.61	98.98	98.72
Mg#	24.8	44.3	30.7	37.7	35.4	29.7	21.3	38.9	38.1	40.5
Na_2O/K_2O	1.74	1.34	1.57	1.54	1.59	1.76	1.31	2.16	1.50	1.43
$Na_2O + K_2O$	7.07	7.73	7.13	7.29	7.1	7.24	7.24	7.05	7.72	7.86
A/CNK	0.88	0.84	0.77	0.87	0.84	0.87	0.91	0.83	0.84	0.84
Trace elements (ppm)										
Ba	858	1,019	831	714	1,038	1,003	1,015	484	787	777
Cr	16	19	14	14	13	15	19	19	17	20
Hf	1.58	1.70	1.32	1.4	1.2	1.63	1.65	2.13	1.58	1.56

Table 3 continued

Pluton sample	Yangxin									
	YX1	YX2	YX3	YX4	YX5	YX6	YX7	YX8	YX9	YX10
Nb	25	19	24	20	21	23	22	23	20	17
Ni	8	10	5	6	6	8	7	7	9	5
Rb	83	88	85	104	87	90	123	85	119	119
Sc	7.3	9.2	11.9	10.3	9.9	7.7	12.2	8.3	8.5	8.9
Sr	1,083	1,058	1,070	964	1,137	1,155	1,053	973	997	1,019
Ta	1.22	0.87	1.29	1.02	1.07	1.18	1.1	1.19	1.07	1
Th	11.8	13.4	12.3	12	9.9	15.6	12.6	26.2	17.9	18.3
U	2.29	3.03	2.47	2.41	2.05	2.99	1.4	5.98	4.06	3.65
V	79	83	85	76	93	84	84	112	98	99
Y	17	15	22	16	19	18	13	21	19	17
Zr	51	62	38	44	39	52	55	73	49	44
La	50.53	42.72	55.83	44.44	48.91	49	47.28	58.46	53.55	48.69
Ce	102.31	88.13	115.87	87.80	100.11	98.66	92.49	112.23	103.45	97.97
Pr	12.23	10.63	13.98	10.59	12.23	11.76	11.24	13.02	12.18	11.84
Nd	41.64	36.89	50.34	35.18	46.97	43.63	42.34	47.13	44.3	41.63
Sm	7.04	6.15	8.48	6.42	7.51	7.14	6.71	8.1	7.35	7.27
Eu	1.85	1.58	2.14	1.64	1.88	1.87	1.75	1.97	1.77	1.77
Gd	5.52	4.92	6.6	5.05	6.23	6.04	4.97	6.34	5.97	5.89
Tb	0.62	0.53	0.74	0.55	0.65	0.62	0.51	0.71	0.63	0.62
Dy	2.98	2.55	3.77	2.79	3.21	3.12	2.35	3.61	3.16	3.07
Ho	0.60	0.5	0.75	0.58	0.66	0.65	0.45	0.75	0.64	0.62
Er	1.64	1.35	2.04	1.51	1.69	1.69	1.12	1.99	1.68	1.63
Tm	0.24	0.19	0.29	0.21	0.24	0.24	0.14	0.28	0.24	0.22
Yb	1.46	1.26	1.82	1.36	1.55	1.51	0.94	1.82	1.53	1.42
Lu	0.21	0.18	0.26	0.19	0.22	0.21	0.13	0.26	0.22	0.20
Sr/Y	63.7	70.4	49.4	59.0	58.7	64.9	81.9	45.9	52.8	59.9
$(La/Yb)_N$	23.4	22.9	20.7	22.1	21.3	21.9	34	21.7	23.6	23.1
Yb_N	8.8	7.6	11	8.2	9.4	9.1	5.7	11	9.3	8.6
Diopside	4.1	6	10.4	4.2	5.6	4.7		6.2	5.8	5.9
Nepheline										
Corundum							0.8			

[a] Sample 00HB-1 from Wang et al. (2004a)

[b] Mg# = [100 × molar Mg/(Mg + Fe)]

[c] A/CNK = molar $Al_2O_3/(CaO + Na_2O + K_2O)$

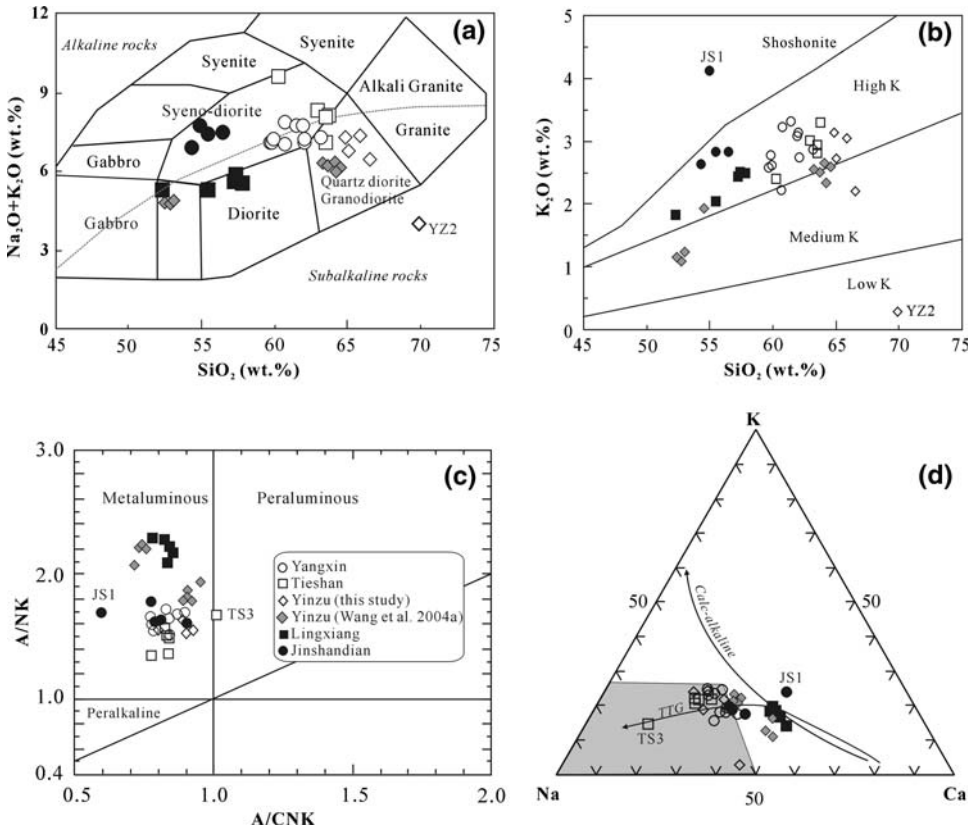

Fig. 5 Geochemical characteristics of the plutonic rocks in the Daye region. **a** Total alkali versus SiO_2 diagram; **b** K_2O versus SiO_2 diagram; **c** A/NK versus A/CNK plot; and **d** Cationic Ca–Na–K diagram. The TTG and CA trends in **d** follow Barker and Arth (1976) and Nockolds and Allen (1953), respectively. A/NK = [molar Al_2O_3/($Na_2O + K_2O$)], A/CNK = [molar Al_2O_3/($CaO + Na_2O + K_2O$)], *TTG* Trondhjemite–Tonalite–Granodiorite, *CA* Calc-Alkaline

Discussions

Large-scale Late Mesozoic magmatism

The present geochronological data demonstrate that the latest Jurassic Yinzu quartz diorite, and presumably together with the undated gabbro-diorite of the Yinzu complex, marks the initiation of Late Mesozoic magmatism in the Daye region. There was a magmatic hiatus of ca. 10 million years until the emplacement of the Lingxiang diorite (141.1 ± 0.7 Ma), which was immediately followed by the formation of the Yangxin (138.5 ± 2.5 Ma) and Tieshan quartz diorite (135.8 ± 2.4 Ma). The Jinshandian diorite (132.4 ± 1.3 Ma) represents the end of major plutonic magmatism, although dykes emplacement persisted. Despite we were not able to date the E'cheng diorite, a phlogopite K–Ar age of 137 Ma (Su and Liu 1994) for the related Cheng-Chao iron skarn deposit (Fig. 2) indicates a similar, early Cretaceous age for its emplacement.

Extensive volcanism took place shortly after the plutonic magmatism in the Daye region. K–Ar dating on biotite and whole-rock samples yielded ages for the volcanism in the 130–113 Ma range (Hubei Bureau of Geology, Mineral Resources 1990; Shu et al. 1992). Recently, Xie et al. (2006) reported a SHRIMP zircon U–Pb age of 128 ± 1 Ma for the Dasi Formation dacite, close to the emplacement ages of the dykes from this study. Collectively, it is concluded that plutonic magmatism in the Daye region started in the late Jurassic (ca. 152 Ma) and peaked in the early Cretaceous (141–132 Ma), which was followed by volcanic eruption and dyke emplacement (Fig. 9a).

Geochronological studies from other regions of the eastern Yangtze craton have yielded results comparable with the Daye regions (Fig. 9b). Similar to Daye, the 151.8 ± 2.6 Ma Shatanjiao quartz monzonite (SHRIMP U–Pb age; Di et al. 2005) represents the earliest magmatic event in the Tongling area (Fig. 1). Pervasive magmatism succeeded in the interval of 142.8 ± 2.2 to 135.8 ± 1.1 Ma, constrained by SHRIMP and LA-ICP-MS zircon U–Pb (Xie et al. 2008, and references therein) and hornblende $^{40}Ar/^{39}Ar$ ages of granitoid plutons (Wu et al. 1996). Similar ages (142.3 ± 1.6–134.7 ± 2.3 Ma) were also obtained for the magmatic rocks and associated ore deposits from the Anqing and Jiurui regions (Fig. 1) (Chen et al. 1991; Wu and Zhou 1997; Mao et al. 2004). The Luzong and Ningwu regions (Fig. 1) are characterized by widespread shoshonitic to high-K calc-alkaline volcanic rocks ranging in composition from basalts to rhyolites, coexisting with small volumes of gabbros, diorites, quartz diorites, syenites, and A-type granites (Chang et al. 1991; Xing and Xu 1994, 1996; Wang et al. 2001; Liu et al. 2002). Available age data indicate that both the volcanic

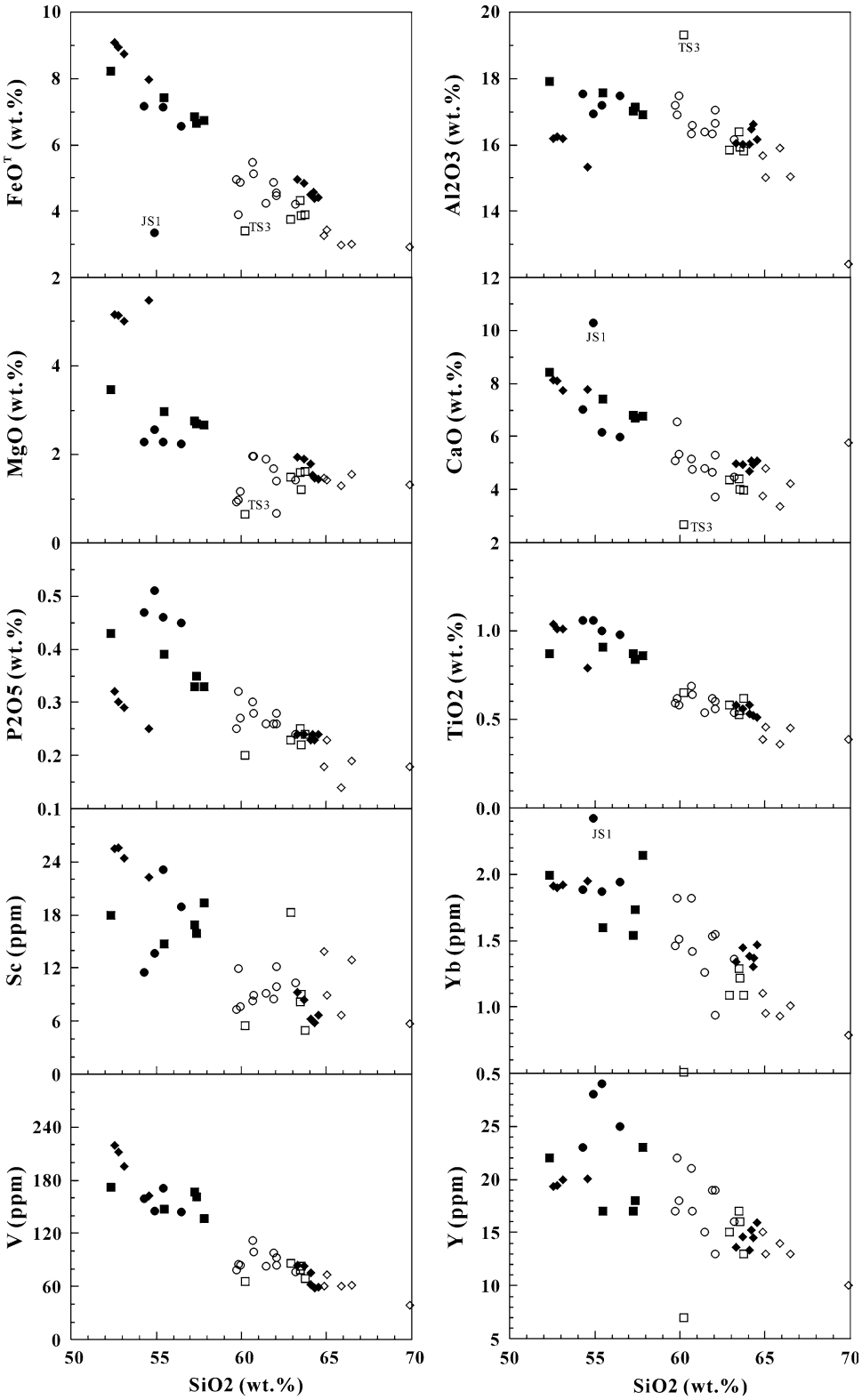

Fig. 6 Selected oxide and trace element Harker's plots for the Daye diorites and quartz diorites. *Symbols* as in Fig. 5

rocks and the mafic and alkaline intrusions were emplaced mainly in the 136–118 Ma range (Xu and Xing 1994; Liu et al. 2002; Wang et al. 2006). Taken together, existing age data demonstrate that extensive magmatism throughout the eastern Yangtze craton was broadly coeval and marked by an early plutonic magmatism of 143–132 Ma and subsequent volcanic eruptions and dyke emplacement during 130–113 Ma (Fig. 9b).

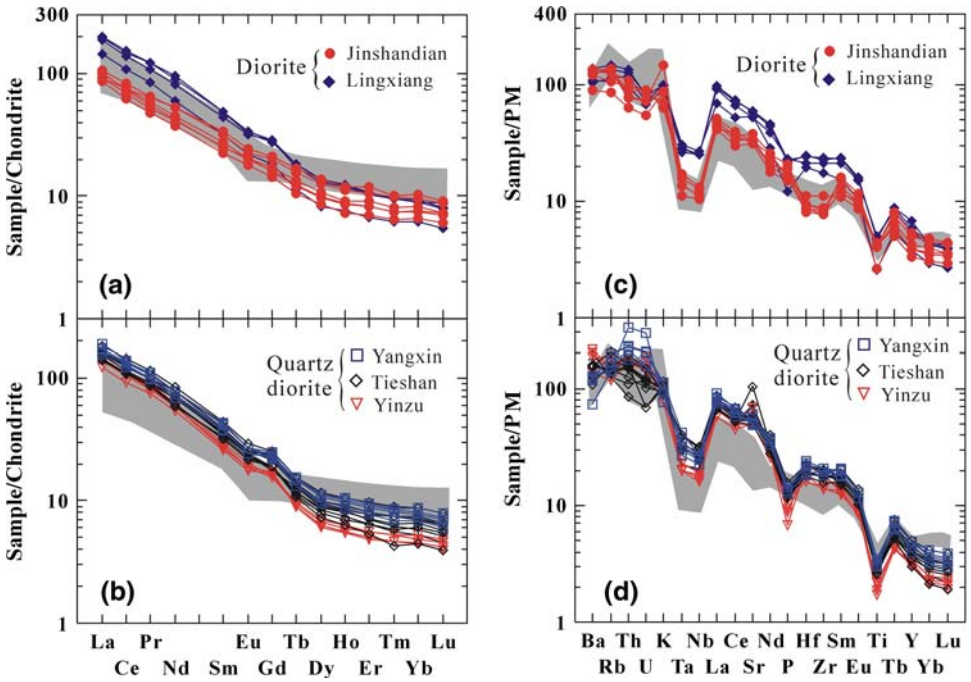

Fig. 7 Chondrite (Boynton 1984) normalized rare earth element patterns (**a**, **b**) and primitive mantle (McDonough and Sun 1995) normalized spiderdiagrams (**c**, **d**) for the plutonic rocks of the Daye region. The *shaded area* denotes the Cretaceous potassic to ultra-potassic basalts from Daye and other regions of the eastern Yangtze craton (Wang et al. 2001, 2006; Liu et al. 2002; Yan et al. 2008)

Petrogenesis of the Daye plutonic rocks

Mantle-derived origin and genetic link between the diorites and quartz diorites

The Sr–Nd isotopic data (Table 4) of the present rocks are strikingly distinct from the Archean basement rocks of the Yangtze craton and the lower crust of both the Yangtze and North China cratons (Fig. 8), precluding their formation by direct remelting of any crustal sources. Instead, the Sr–Nd isotopes are indistinguishable from the contemporaneous, mantle-derived basalts (130–120 Ma) and mafic intrusions (143–125 Ma) of the eastern Yangtze craton (Wang et al. 2001, 2006; Liu et al. 2002; Yan et al. 2008). Combined with the geochemical features (Figs. 5, 6, 7), we suggest that intrusions from the Daye region were most likely generated by partial melting of an enriched mantle source. This is corroborated by the similarity of Sr–Nd isotopes between the Daye intrusions and an EM-II source that has resulted from metasomatism of subcontinental lithospheric mantle by hydrous slab melts or fluids (Geldmacher et al. 2008). The homogeneous isotopic compositions of individual intrusions (Table 4) and lack of a correlation between SiO_2 and $\varepsilon_{Nd}(t)$ values (not shown) also indicate that assimilation of crustal materials, if any, was not evident in the magmatic process. This is partly confirmed by the lack of old inherited zircons in light of both CL images and spot U–Pb analyses of zircon grains (Figs. 3, 4).

It is noted that both diorites and quartz diorites have prominent negative Nb–Ta anomalies (Fig. 7c, d), typical signature of subduction-related magmas (Sajona et al. 1993). When normalized to the average of oceanic plagiogranites (ocean ridge granite) reported by Pearce et al. (1984), the rocks resemble arc granites but clearly differ from within-plate granites (not shown). This seems to indicate that the rocks have an arc affinity. Such anomalies, however, were also frequently observed in rocks derived from enriched subcontinental lithospheric mantle (Whalen et al. 1996; Jahn et al. 1999). Absence of arc magmatism in the Daye region implies that the observed Nb–Ta anomalies reflect an enriched lithospheric mantle source that resulted from interactions with subduction-related melts and/or fluids. The radiogenic Sr–Nd isotopic data of the Daye rocks, which are compatible with the contemporaneous, mantle-derived potassic to ultra-potassic basalts and mafic intrusions (Fig. 8), confirm this view. The early Cretaceous basalts and mafic intrusions over the eastern Yangtze craton all display an enriched-mantle affinity (Wang et al. 2001, 2006; Liu et al. 2002, 2006; Xie et al. 2006; Yan et al. 2008), demonstrating that modification of the mantle beneath the eastern Yangtze craton has been pervasive. Timing and nature of the subduction and related metasomatism are not clear, but we envisage two possible causes here. One is the collision of the Cathaysia block towards the Yangtze craton during the ca. 1,000-Ma Jinning orogeny (Yang et al. 1986). The other may relate to the Mesozoic flat-slab subduction of the paleo-Pacific plate of ca. 1000 km diameter underneath the eastern China continent, beginning at middle Jurassic (Zhou and Li 2000) or early Triassic (Li and Li 2007).

Table 4 Sr–Nd isotopic compositions of magmatic rocks from the Daye region

Sample	Rb (ppm)	Sr (ppm)	$^{87}Rb/^{86}Sr$	$^{87}Sr/^{86}Sr$	$^{87}Sr/^{86}Sr(t)$	Sm (ppm)	Nd (ppm)	$^{147}Sm/^{144}Nd$	$^{143}Nd/^{144}Nd$	$^{143}Nd/^{144}Nd(t)$	$\varepsilon_{Nd}(t)$	T_{DM} (Ga)
Yinzu quartz diorite, $t = 151.8$ Ma												
L4	6.7	1,128	0.0172	0.706911	0.7069	1.97	12.73	0.0937	0.512317	0.512237	−4.55	1.1
L6	25.3	3,659	0.0200	0.707216	0.7072	1.59	10.78	0.0894	0.51234	0.512264	−4.03	1.0
Tieshan quartz diorite, $t = 135.8$ Ma												
TS2	28.3	2,799	0.0292	0.707645	0.7076	3.22	19.69	0.0988	0.512109	0.512025	−8.70	1.4
TS4	21.4	2,753	0.0224	0.707177	0.7071	5.64	40.12	0.0918	0.512112	0.512034	−8.52	1.3
TS5	33.5	1,431	0.0675	0.706343	0.7062	4.10	22.98	0.1077	0.512355	0.512263	−4.05	1.1
TS6	13.8	1,477	0.0270	0.706073	0.7060	3.48	23.25	0.0905	0.512206	0.512129	−6.67	1.2
Yangxin quartz diorite, $t = 138.9$ Ma												
YX4	5.5	1,747	0.0090	0.706918	0.7069	2.23	12.22	0.1100	0.512388	0.512294	−3.44	1.1
YX5	21.1	3,087	0.0197	0.706542	0.7065	7.43	46.56	0.0967	0.512269	0.512187	−5.54	1.1
YX6	16.7	1,007	0.0478	0.706206	0.7061	1.27	8.26	0.0928	0.512204	0.512125	−6.74	1.2
YX8	32.9	2,532	0.0374	0.706201	0.7061	3.49	21.87	0.0964	0.512244	0.512162	−6.02	1.2
Lingxiang diorite, $t = 141.1$ Ma												
LX1	72.0	656	0.3178	0.708899	0.7083	4.83	24.30	0.1202	0.512259	0.512148	−6.02	1.45
LX2	75.5	630	0.3468	0.709754	0.7091	5.06	25.73	0.1189	0.512233	0.512123	−6.50	1.47
LX3	71.4	659	0.3132	0.708516	0.7079	4.76	24.89	0.1156	0.512211	0.512104	−6.87	1.46
Jinshandian diorite, $t = 132.4$ Ma												
JS1	92.1	1,377	0.1935	0.706468	0.7061	10.45	56.18	0.1124	0.512312	0.512215	−4.93	1.26
JS2	59.6	930	0.1852	0.706225	0.7059	8.40	48.65	0.1044	0.512109	0.512019	−8.77	1.45
JS3	55.1	981	0.1624	0.706112	0.7058	7.83	44.46	0.1065	0.512210	0.512118	−6.82	1.33
Tongshankou granodiorite, $t = 141$ Ma												
TSK03	87.3	512	0.4910	0.707345	0.7063	5.29	34.13	0.0938	0.512314	0.512226	−4.44	1.06
TSK04	133	900	0.4248	0.707108	0.7062	5.79	35.98	0.0974	0.512321	0.512230	−4.37	1.09
TSK05	97	786	0.3572	0.706977	0.7063	5.28	29.80	0.1073	0.512317	0.512217	−4.63	1.19
TSK06	219	927	0.6808	0.708037	0.7067	5.85	35.03	0.1011	0.512317	0.512223	−4.51	1.13
Dasi Formation dacites and basalts, $t = 128$ Ma												
DSZ4	150	443	0.9840	0.708998	0.7072	9.01	54.80	0.0990	0.512147	0.512064	−7.98	1.23
DSZ5	150	421	1.0320	0.708985	0.7071	7.54	50.90	0.0900	0.512150	0.512075	−7.78	1.33
DSZ12	55.5	587	0.2740	0.707070	0.7066	5.86	32.50	0.1090	0.512255	0.512164	−6.04	1.30

[a] $(^{87}Rb/^{86}Sr)_t$ and $\varepsilon_{Nd}(t)$ were calculated with modern $(^{143}Nd/^{144}Nd)_{CHUR} = 0.512638$ and $(^{147}Sm/^{144}Nd)_{CHUR} = 0.1967$ and T_{DM} were calculated using present-day $(^{147}Sm/^{144}Nd)_{DM} = 0.2137$ and $(^{143}Nd/^{144}Nd)_{DM} = 0.51315$

[b] Data of the Tongshankou granodiorite and the Dasi Formation dacites and basalts were from Li et al. (2008) and Xie et al. (2006)

The similarity in chondrite-normalized REE and the primitive mantle-normalized trace element patterns (Fig. 7) and the well comparable Sr–Nd isotopic compositions (Fig. 8) between the diorites and quartz diorites indicate that they are genetically related. The linear or sub-linear trend of selected major and trace elements in the Harker diagrams (Fig. 6) demonstrate that the quartz diorites may have been formed via fractional crystallization of magmas represented by the diorites. Close temporal and spatial relations of diorites and quartz diorites provide additional weight of evidence for their genetic link. For example, the Lingxiang diorite (141.1 ± 0.7 Ma) and the Tongshankou granodiorite (140.6 ± 0.6 Ma; Li et al. 2008) were emplaced simultaneously in close proximity (Fig. 2).

Genesis of the diorites

As discussed earlier, the dioritic rocks in the Daye region were most likely derived from an enriched mantle source. However, direct partial melts of such a source would be of basaltic composition rather than andesitic (Nicholls and Ringwood 1972; Green 1973; Wilson 1989). Although experimental data showed that silica-rich melts might be produced by small degree partial melting of mantle peridotite (Baker et al. 1995), $Mg^{\#}$ of such melts in equilibrium with mantle olivine would range from 70 to 80 (Falloon et al. 1997). Much lower $Mg^{\#}$ is seen for the Lingxiang and Jinshandian diorites (Table 3), indicating that the rock compositions measured cannot represent primary melts that

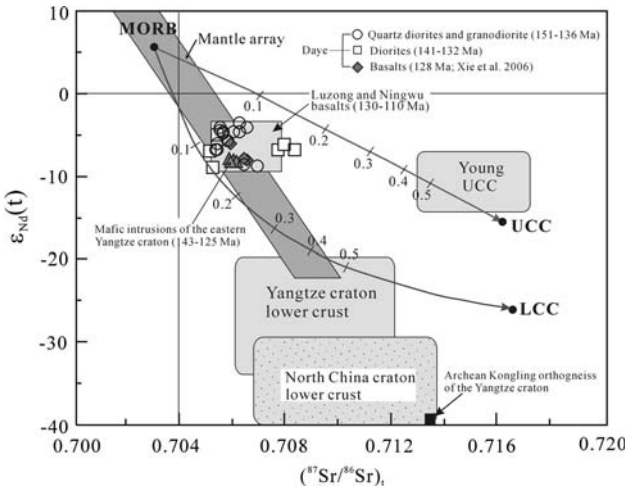

Fig. 8 Initial $^{87}Sr/^{86}Sr$ versus $\varepsilon_{Nd}(t)$ for the Daye diorites and quartz diorites. Reference data sources: Dasi Formation basalts (Xie et al. 2006), Luzong and Ningwu basalts (Wang et al. 2001, 2006; Liu et al. 2002), mafic intrusions of the eastern Yangtze craton (Yan et al. 2008), Archean Kongling gneiss (Ames et al. 1996), upper continental crust (*UCC*; Taylor and McLennan 1985). Other fields cited from Jahn et al. (1999). Also shown are the mixing calculations for source and melt contaminations using the parametric equations 13.5 of Faure (1986). The mixing hyperbolas were modeled by mixing average compositions of lower continental crust (*LCC*) and UCC (Rollinson 1993; Rudnick 1995) with those of N-MORB (Rollinson 1993; Sun and McDonough 1989). See Fig. 2 for locations of referenced areas

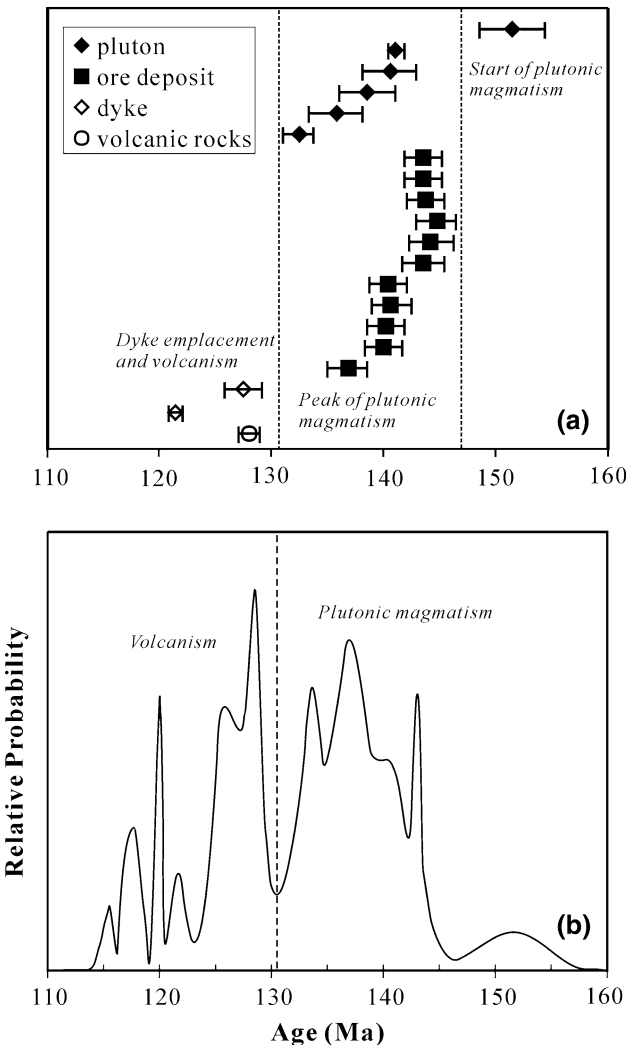

Fig. 9 Age distribution of the Late Mesozoic magmatic rocks in the Daye region (**a**) and other regions of the eastern Yangtze craton (**b**). See text for data sources and explanations

were in equilibrium with peridotitic mineral assemblages. The low Cr and Ni contents in the samples (Table 3) are compatible with this view. We therefore suggest that the present dioritic rocks represent differentiated liquids that evolved from a parental basaltic magma by fractional crystallization of olivine in depth.

Geochemical modeling was performed to examine the genesis of the Daye diorites by partial melting of peridotitic mantle and subsequent olivine crystallization. During the modeling, three mantle compositions were chosen: (1) DM (depleted mantle) with $Yb_N = 2.9$ and $(La/Yb)_N = 0.5$ (McCulloch and Bennett 1994); (2) EM (slightly enriched mantle) with $Yb_N = 3.5$ and $(La/Yb)_N = 6.2$ (Graviou et al. 1988), and (3) RS1, a phlogopite- and pargasite-bearing lherzolite sample with $Yb_N = 2$ and $(La/Yb)_N = 11.3$ (Menzies et al. 1987). For trace element modeling, we applied the Shaw's batch melting equation $C_L = C_O/[D + F(1-D)]$ (Shaw 1970), where C_O and C_L are trace element abundances respectively in the source and liquid, D means bulk partition coefficients, and F denotes degree of partial melting. The partition coefficients were taken from the GERM *Kd* database (Nielsen 2006).

Figure 10a illustrates the curves for partial melting of DM (with 5% spinel and 6% garnet), EM and sample RS1 (5% spinel, 6% garnet plus 2% amphibole and 2% phlogopite). It is clear that partial melting of a depleted mantle, regardless the residual mineral assemblage, cannot generate magmas with La/Yb ratios as high as observed in the Daye diorites. The more likely source thus would be an enriched mantle source. Most samples of the Jinshandian diorite may be explained by 22% partial melting of enriched mantle equivalent in composition to sample RS1, following considerable amounts of olivine fractionation (Fig. 10a). However, sample JS1, which differs from other samples by high CaO, Ba, Hf, Rb, Sr, Ta, U, low Na_2O/K_2O and presence of normative nepheline (Table 3), corresponds to 20% olivine fractionation from a parental magma generated by 17% partial melting of EM. The Yinzu gabbro-diorite would require 35% fractional crystallization from a parental magma derived from 36% partial melting of an EM source. Samples of the Lingxiang diorite might be explained by variable degree of partial melting of an EM source, with different amounts of olivine fractionation of the partial melt. Coexistence of diorites and

broadly coeval basalts, together with abundance of mafic enclaves in the Lingxiang diorite, support the geochemical modeling results.

Other experimental studies demonstrated that diorites might be formed through partial melting of an oceanic crust (Rushmer 1991; Sen and Dunn 1994; Rapp and Watson 1995). The same modeling procedure was applied to test the possibility of this mechanism in the formation of the Daye diorites, assuming the mafic source with $(La/Yb)_N = 5$ and $Yb_N = 6–17$ (Fig. 10b). It appears that the Lingxiang diorites may be generated by ~30% partial melting of an oceanic crust transformed into garnet-free amphibolite. However, when applying this degree of partial melting of an amphibolite source (N-MORB: 35.8 ppm Y and 113 ppm Sr; Hofmann 1988) to the batch melting equation of Shaw (1970), the expected melt has 33 ppm Y, 140 ppm Sr, and Sr/Y ratio of 4, which are distinctly different from the Lingxiang diorites (17–23, 634–749, and 30–39 ppm, respectively). Moreover, experimental studies have shown that partial melting of low-K tholeiites under both water-saturated and water-undersaturated conditions generate liquids that are peraluminous or transitional between metaluminous and peraluminous (Beard and Lofgren 1991), which is in contrast with the metaluminous nature of the Lingxiang diorites (A/CNK <0.84, without normative corundum).

In light of the results of geochemical modeling and the Sr–Nd isotope data, we conclude that the Daye diorites were derived from an enriched mantle source. Composition of the source can be calculated by mixing DM (Workman and Hart 2005) with different proportions of low-silica adakites (LSA), high-silica adakites (HSA), Archean TTGs, and sanukitoids (Martin et al. 2005). The best results were obtained for a metasomatised mantle (MM) produced by mixing 90% DM and 10% HSA. Samples of both Jinshandian and Lingxiang diorites and gabbro-diorite of the Yinzu complex have trace element patterns parallel to the MM (Fig. 11), providing an additional argument for this common source. The patterns agree well with the formation of the Daye diorites by ~15–25% partial melting of a slab-melt modified mantle source, followed by 40–70% fractional crystallization of olivine at mantle depth, consistent with results shown in Fig. 10a. Occurrences of ophiolites in the southeastern margin of the Yangtze craton and the 968-Ma slab-derived Xiwan adakites that intruded the ophiolites provide direct geological evidence for an ancient oceanic crust subduction process and hence mantle metasomatism by slab melts and/or fluids (Li and Li 2003).

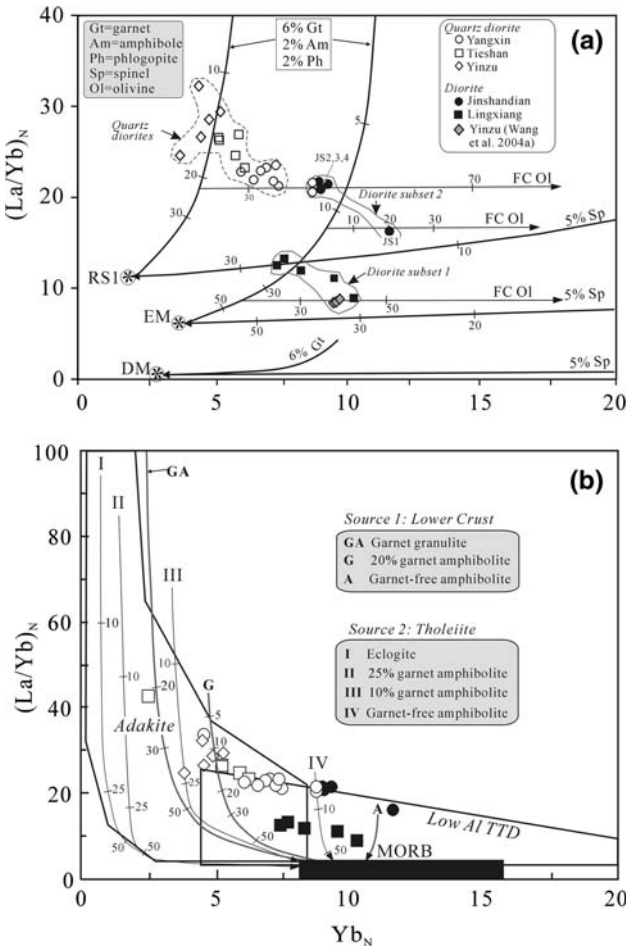

Fig. 10 Chondrite-normalized (Sun and McDonough 1989) (La/Yb) versus Yb diagrams for the Daye diorites and quartz diorites. **a** Partial melting curves of DM (5% Spinel 6% Gt), EM and sample RS1 (5% spinel, 6% garnet plus 2% amphibole and 2% phlogopite). Labeled tick marks indicate per cent partial melting of spinel- and garnet-bearing model curves and fractional crystallization of olivine (FC Ol). **b** Partial melting curves of lower crust and tholeiitic oceanic crust leaving garnet or amphibole in the residue, calculated by using Shaw's batch melting equation (Shaw 1970) and partition coefficients in Martin (1987), Rollinson (1993) and Nielsen (2006). The fields of adakites and low Al TTD are from Drummond and Defant (1990). *Other symbols* as in Fig. 6. *Other symbols* as in Fig. 6. See text for explanation. *DM* depleted mantle, *EM* enriched mantle, *RS1* garnet peridotite sample in Menzies et al. (1987), *TTD* Trondhjemite–Tonalite–Dacite

Genesis of the quartz diorites

A striking feature of the quartz diorites is that they have geochemical signatures similar to adakites, such as high Sr, Al_2O_3, Na_2O/K_2O, low Y, Yb, Sc, and high Sr/Y and La/Yb ratios (Table 3). Adakites are a class of intermediate to acidic volcanic or plutonic rocks characterized by high Sr (>400 ppm), Sr/Y (>40) and La/Yb (>20), and low Y (<18 ppm) and Yb (<1.9 ppm) (Defant and Drummond 1990). They have been interpreted to be products of partial melting of young subducting oceanic crust, with hybridization of the slab melts with mantle peridotite while they ascend (Kay 1978; Defant and Drummond 1990; Sajona et al. 1993; Peacock et al. 1994). Recent studies have also

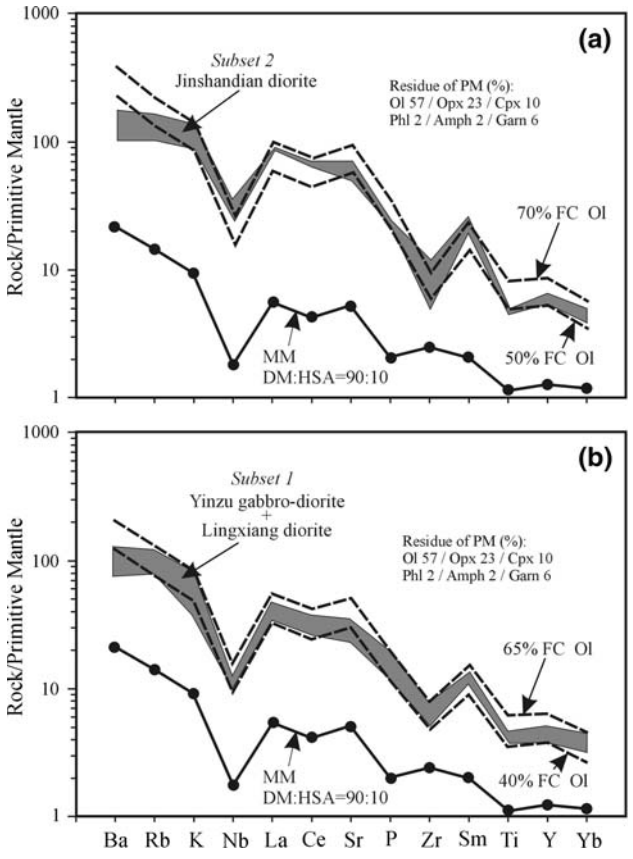

Fig. 11 Primitive mantle normalized (Sun and McDonough 1989) multi-elemental diagrams for the Daye diorites and the metasomatised mantle (*MM*). The MM is assumed as mixing of 90% deplete MORB mantle (Workman and Hart 2005) with 10% slab-derived melt having high-silica adakite (HSA) composition (Martin et al. 2005). The modeling was based on the Shaw's batch melting (Shaw 1970) and Rayleigh fractional crystallisation equations (Rayleigh 1896). The partition coefficients are from Martin (1987), Rollinson (1993) and Nielsen (2006). The modeling was performed assuming a two-stage process: (1) partial melting of a MM source, and (2) fractional crystallization of olivine in the resultant magma. The MM source is assumed to have phlogopite (2%), amphibole (2%), garnet (0–5%), and spinel (0–5%) as accessory phases

shown that many igneous rocks possess geochemical features similar to adakites but are apparently unrelated to slab melting. These are termed as adakitic rocks as suggested by Castillo (2006). Alternative mechanisms have been proposed to explain the generation of adakitic rocks. These mainly include (1) partial melting of a peridotitic mantle that has been modified by slab melts (Martin et al. 2005, and references therein), (2) melting of thickened (Chung et al. 2003; Petford and Atherton 1996; Wareham et al. 1997) or delaminated mafic lower crust (Kay and Kay 1993; Xu et al. 2002; Gao et al. 2004), and (3) fractional crystallization of mantle-derived magmas (Castillo et al. 1999; Macpherson et al. 2006).

Some of the quartz diorite samples in the Daye region appear to fit partial melting curves of a tholeiitic source metamorphosed to garnet-free amphibolite to 10% garnet amphibolite (Fig. 10b). These rocks, however, have radiogenic Sr–Nd isotopic compositions (Table 4; Fig. 8), indicating that a slab-melting model is not feasible for their genesis as slab-derived adakites are generally characterized by primitive Sr and Nd isotopes ($^{87}Sr/^{86}Sr < 0.7045$) (Kay 1978; Defant and Drummond 1990; Bourdon et al. 2002). Lack of coeval arc magmatism in the Daye region also argues against a slab-melting model. Moreover, slab melts would acquire elevated MgO contents and $Mg^{\#}$ via interactions with mantle peridotite during their ascent (Martin et al. 2005). The opposite is observed in the Daye quartz diorites, which have much lower MgO (0.6–2.0 wt.%) and $Mg^{\#}$ (21–48) (Table 3) relative to slab-derived adakites.

Adakitic rocks by partial melting of a peridotitic mantle wedge whose composition has been modified by reactions with felsic slab-melts were termed as LSA, marked by low silica (56 wt.%), high MgO (5.15 wt.%) and $Mg^{\#}$ (61), and elevated Cr (157 ppm) and Ni (103 ppm) contents (Martin et al. 2005). The adakitic rocks in the Daye region show different compositions compared to LSA, containing higher silica (60–71 wt.%) but much lower MgO (0.68–1.96 wt.%), $Mg^{\#}$ (21–48), Cr (12–31 ppm) and Ni (5–28 ppm). High-Mg andesites, commonly associated with adakitic rocks by partial melting of mantle peridotite contaminated by slab melts (Tatsumi 2006), are also lack in either Daye or other magmatic regions of the eastern Yangtze craton. These suggest that the present adakitic rocks cannot represent the direct melts of peridotitic mantle metasomatised by slab-derived magma.

Generation of adakitic rocks via partial melting of thickened basaltic lower crust where garnet is a stable and residual phase has been demonstrated by experimental studies of hydrous metabasalt at high *P–T* conditions (Rapp et al. 1991; Sen and Dunn 1994; Rapp and Watson 1995) and examined in several localities (Atherton and Petford 1993; Muir et al. 1995; Chung et al. 2003). This mechanism was also introduced to explain the genesis of the Yinzu quartz diorite (Wang et al. 2004). The present crustal thickness of the Daye region is merely 30–31 km (Zhai et al. 1992). Considering that the volcanic associations and shallow-seated porphyry ore deposits in the region have been well-preserved (Shu et al. 1992; Li et al. 2008), it is reasonable to assume a magnitude of denudation less than 3–4 km since the early Cretaceous. This indicates that the early Cretaceous crustal thickness in the Daye region must not be more than 40 km, condition insufficient for the lower crust to be transformed into garnet amphibolite or eclogite. In addition, lack of eclogite or eclogite-bearing assemblages throughout the eastern Yangtze craton, either as outcropped blocks or xenoliths entrained in Cretaceous basalts, does dot support existence of eclogitized lower crust and thus its melting as an effective way to generate the adakitic rocks.

Wang et al. (2004) invoked partial melting of delaminated lower crust in the mantle lithosphere or thickened mafic lower crust to explain the genesis of the adakite-like Yinzu quartz diorite and the Tongshankou granodiorite (Fig. 2). Melts of delaminated lower crust will inevitably interact and equilibrate with the mantle peridotite while they ascend, resulting in significantly elevated concentrations of Cr, Ni, and MgO (Rapp et al. 1999; Gao et al. 2004). The low abundances of these elements in the present adakitic rocks are inconsistent with such interactions. The Daye region has long been regarded as a backland area of the Dabie Orogen (Hubei Bureau of Geology, Mineral Resources 1990), indicating that it had much thinner crust than the latter during the early Cretaceous when the adakitic intrusions were formed. This in turn implies that the Daye area was less susceptible to delamination of lower crust than the Dabie Orogen at that time. Interestingly, the 143–142-Ma adakitic intrusions from the core of the Dabie Orogen that contain low to very low Cr (2.1–24 ppm) and Ni (1.4–9.6 ppm) have been demonstrated to be formed by partial melting of thickened lower crust, rather than delaminated lower crust (Wang et al. 2007). This indicates that the lower crust of the Dabie Orogen was not significantly delaminated during the earliest Cretaceous. In this regard, we infer that the adakitic intrusions of the Daye region were less likely to be produced by partial melting of delaminated lower crust.

Preclusion of those three possibilities led us to favor fractional crystallization of mantle-derived parental magmas (Castillo et al. 1999; Macpherson et al. 2006) to explain the genesis of the Daye adakitic rocks. Richards and Kerrich (2007) stressed that the key adakitic geochemical signatures, notably low Y and Yb concentrations and high Sr/Y and La/Yb ratios, are more frequently generated by this mechanism. Selected Harker plots (Fig. 6) confirm that fractional crystallization has been important in the magmatic processes, with removal of Al-, Fe-, Mg-, Ca-, Ti-, P-, Y-, Yb- and V-rich phases such as hornblende, plagioclase, magnetite and apatite. The SiO_2 versus Sr/Y and Yb_N diagrams (not shown), where the values of Yb_N decrease and Sr/Y increase with increasing SiO_2, are consistent with such a mechanism in generating the adakitic quartz diorites. When the most incompatible elements Ba and Rb are plotted against the compatible element Ni (Fig. 12), a fractional crystallization trend becomes more evident. Such a trend is indicative of fractionation of hornblende and magnetite that have partition coefficients for Ni much greater than 1 in intermediate to acidic liquids (Nielsen 2006). Fractionation of hornblende and plagioclase also agrees with the slightly negative Eu anomalies in quartz diorites (Fig. 7b).

To provide more details on the fractional process, we performed geochemical modeling by employing a classical

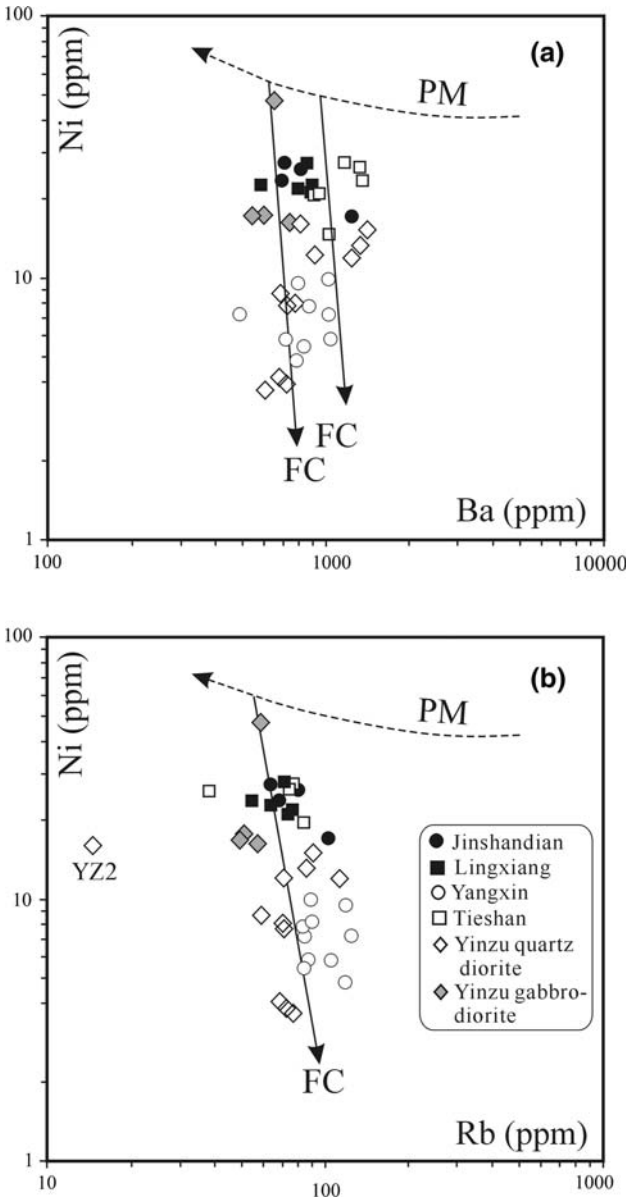

Fig. 12 Plots of the most incompatible elements Ba and Rb versus the compatible element Ni, indicating that fractional crystallization (*FC*), rather than partial melting (*PM*) dominated the genesis of the adakitic quartz diorites of the Daye region. Data of the Yinzu quartz diorite are from Wang et al. (2004) and this study, while the Yinzu gabbro after Wang et al. (2004)

mass-balance equation system that was solved using the algorithm of Störmer and Nicholls (1978). The theoretical modeling was performed assuming the differentiation of a parental magma (C_O) into an evolved/differentiated liquid (C_L). The accuracy of the adjustment of the theoretical model to the data is expressed by the sum of the squares of the residuals $\Sigma r^2 = \Sigma(m_i - c_i)^2$, where m_i and c_i denote measured and calculated concentrations of oxide i, respectively. The mineral compositions used in the calculation were from Deer et al. (1983). Because (1) the Yinzu

complex (151.8 Ma) consists of gabbro-diorite and quartz diorite that were emplaced at least 10 Myr earlier than the other intrusions (141–132 Ma), and (2) the Jinshandian diorite is somewhat different in geochemistry from the Lingxiang diorite and the Yinzu gabbro-diorite (Figs. 5, 10), we divided the diorites into two subsets, with the Lingxiang diorite plus Yinzu gabbro-diorite as subset 1 and the Jinshandian diorite as subset 2. Accordingly, we modeled the formation of the Yinzu quartz diorite by fractional crystallization of the Yinzu gabbro-diorite (group A) and formation of the Tieshan quartz diorite by fractional crystallization of the Jinshandian diorite (group B), separately. To model the behavior of the group A, sample 01YZ-4-1 (Wang et al. 2004) was chosen as C_O and YZ3 as C_L, whereas JS3 and TS2 are C_O and C_L for group B. The composition of both C_O and C_L were recalculated to 100% on anhydrous basis; but MnO was not considered as its concentration is negligible (Table 3).

The results for the modeling of both groups are shown in Table 5. The best fit of computed model to the analytical data is obtained for crystallization of a mineral assemblage of hornblende, plagioclase, magnetite and traces of apatite for group A, and of hornblende, plagioclase, K-feldspar, magnetite and apatite for group B; the degree of fractional crystallization is 64 and 56%, respectively. In group B, the behavior of Zr is accounted for only when small amounts (0.03%) of zircon are added in the fractional phases. The calculated cumulates are consistent with the inferred fractional assemblages from the Harker diagrams (Fig. 6) and agree with the major phenocryst phases observed in the quartz diorites. The reliability of the modeling is indicated by the calculated oxide contents (C_L') that agree well with the observed values of the selected samples YZ3 and TS2, with statistical error (Σr^2) of 0.2 and 0.7 (Table 5). The second step in quantification of fractional crystallization is to reintroduce the computed modal compositions of the

Table 5 Major and trace element modeling for the Daye intrusions

Sample	Group A[a]			Group B[a]		
	C_O 01YZ-4-1 [b]	C_L YZ3	CL′ FC = 64%	C_O JS3	C_L TS2	CL′ FC = 56%
Major oxides (wt.%)						
SiO_2	53.53	67.5	67.56	55.68	64.28	64.44
TiO_2	1.06	0.37	0.34	1.09	0.59	0.13
Al_2O_3	16.5	16.3	16.3	17.97	16.19	16.31
$Fe_2O_3^t$	10.14	3.4	3.45	8.16	4.24	4.66
MgO	5.27	1.32	1.37	2.35	1.51	1.09
CaO	8.27	3.45	3.42	7.2	4.46	4.74
Na_2O	3.7	4.4	4.53	4.36	5.43	5.28
K_2O	1.2	3.12	2.76	2.71	3.07	3.15
P_2O_5	0.33	0.14	0.26	0.48	0.23	0.2
Trace element (ppm)						
Ba	594	1,404	1,217	710	1,164	1,023
La	22.9	44.7	46	58.3	43	45
Nb	7.3	17	22	18	15	17
Ni	63	15	8	28	28	14
Rb	51	90	101	63	76	107
Sr	539	1,382	1,085	1,041	1,440	1,125
Y	19	14	8	23	15	15
Yb	1.9	0.9	1	1.9	1.1	1.1
Zr	60	114	126	66	54	49
Cumulate (%)						
Hornblende			73.8			36.2
Plagioclase (An_{40})			24.8			46.2
K-feldspar			–			10.1
Magnetite			1.3			6.1
Apatite			0.1			1.4
Zircon			–-			0.03
FC (%)			64			56
Σr^2			0.2			0.7

C_O and C_L: less and more evolved samples, respectively. C_L': calculated liquid composition after extraction of cumulates. *FC* per cent of fractional crystallization

[a] Group A consists of the Yinzu gabbro-diorite and quartz diorites; Group B comprises the Jinshandian diorite and the Yiangxin and Tieshan quartz diorite

[b] Data after Wang et al. (2004)

cumulate and the degree of fractional crystallization in trace element modeling. The equation chosen for fractional crystallization is that of Rayleigh (1896): $C_L = C_O \times F^{(D-1)}$, where C_L is the calculated concentration of a trace element in the differentiated liquid, C_O is the concentration of a trace element in the parental magma, $F = 1 - FC$ (FC is the degree of fractionation, with $0 < FC \leq 1$) and D is the bulk distribution coefficient (Rollinson 1993). For 64% (group A) and 56% (group B) fractional crystallization, the calculated trace element contents show perfect agreement with the analytical values (Table 5). The modeling results are corroborated by the very good fit of the present samples to fractional crystallization curves in the Y versus Sr/Y and normalized Yb versus La/Yb diagrams (Fig. 13). Coexistence of adakitic quartz diorite and non-adakitic gabbro-diorite in the Yinzu complex and presence of mafic enclaves in the Tieshan and Lingxiang intrusions, consisting of plagioclase, hornblende, biotite, pyroxene, and K-feldspar, and accessory titanite, magnetite, and apatite, lend additional support to fractional crystallization in the formation of quartz diorites.

Figure 14 illustrates the petrogenetic model for the plutonic rocks of the Daye region. We envisage four stages in their genesis: (1) an early episode of hybridization, in which the depleted mantle was metasomatised by slab melts (HAS); (2) ~15–40% partial melting of this metasomatised mantle, generating basic magmas that evolved by (3) 40–70% fractional crystallization of olivine at mantle depth, forming the Daye diorites; and (4) low pressure fractional crystallization of cumulates composed of amphibole + plagioclase ± K-feldspar + magnetite + apatite ± zircon, resulting in the adakitic quartz diorites.

Regional synthesis and geodynamic implications

Combined with previous isotopic ages, the present geochronological data suggest that pervasive magmatism in the Daye region and throughout the eastern Yangtze craton took place coevally in the latest Jurassic to early Cretaceous (Fig. 9). Voluminous and broadly synchronous magmatism is also widespread in the eastern part of the Cathaysia block (Zhou and Li 2000), in the Dabie-Sulu Orogen (Ma et al. 1998; Jahn et al. 1999; Xu et al. 2007), and in the northern and eastern margins of the North China craton (Wu et al. 2005a, b), forming a huge NNE-striking magmatic belt in eastern China. The geochemical and Sr–Nd isotope data of the magmatic rocks, together with the coexistence of coeval felsic to mafic rocks, indicates large scale melting of subcontinental lithospheric mantle during the Late Mesozoic time. Mafic granulite xenoliths entrained in Cenozoic basalts from several localities around eastern China are considered as analogue of mantle-derived magmas ponded at the base or lower part of crust

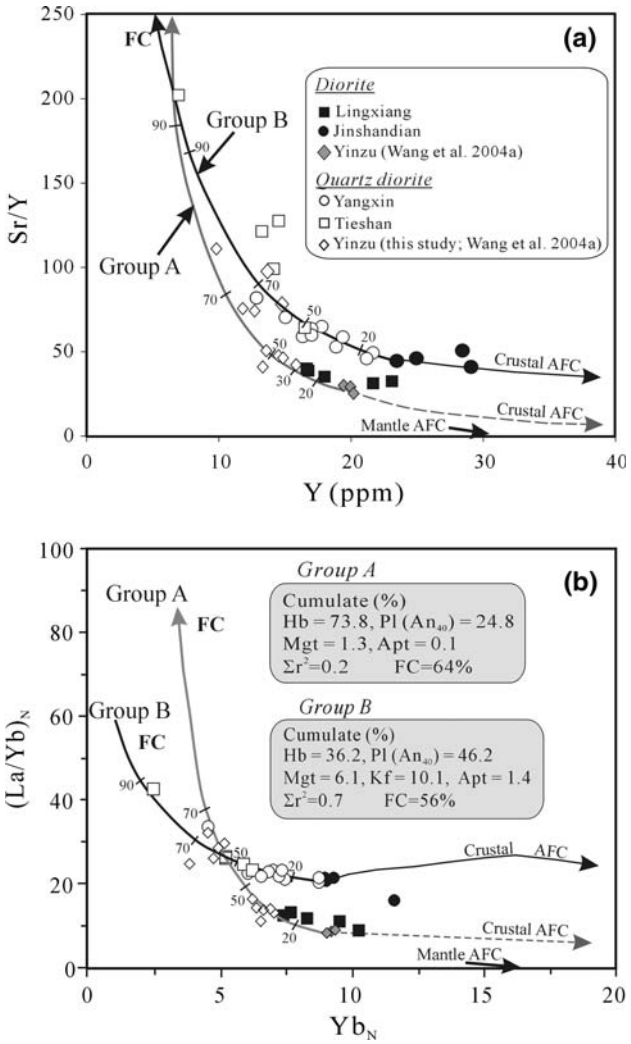

Fig. 13 Y versus Sr/Y (**a**) and Yb_N versus $(La/Yb)_N$ (**b**) diagrams illustrating the genesis of the quartz diorites via fractional crystallization (*FC*) of mainly hornblende plus plagioclase from parental dioritic magmas similar in composition to the Yinzu, Lingxiang or Jinshandian diorites. In both figures, curves of mantle and crustal assimilation and fractional crystallisation (*AFC*) were calculated following DePaolo (1981). For mantle AFC we used a MORB-like (Sun and McDonough 1989) magma and the lower continental crust (Rudnick and Fountain 1995) as contaminant. For crustal AFC, we used the Yinzu gabbroic–diorite and the Jinshandian diorite as original liquid and the lower continental crust as contaminant. In the AFC models, we considered mass-assimilation ratios of 2 and 1.5 for mantle and crustal AFC, and 80% (20%) amphibole and 60% (40%) plagioclase as fractionating phases, respectively

(Yu et al. 2003; Huang et al. 2004). SHRIMP zircon U–Pb dating has constrained crystallization of the protolith of the granulite xenoliths mainly in the 159–120 Ma range (Fan et al. 1998; Wilde et al. 2003; Huang et al. 2004), coincident with the timing of extensive magmatism in the eastern Yangtze craton and the entire eastern China continent. Widespread occurrences of strong, sub-horizontal, continuous layered seismic reflectors in the lower crust beneath

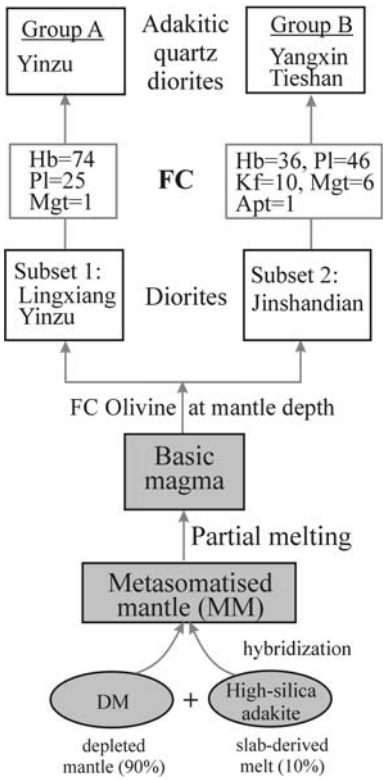

Fig. 14 Schematic diagram showing the successive petrogenetic processes that gave rise to the plutonic rocks of the Daye region. *MM* metasomatised mantle; *DM* depleted mantle; *FC* fractional crystallization; *PM* partial melting; *Ol* olivine; *Hb* hornblende; *Pl* plagioclase; *Kf* K-feldspar; *Mgt* magnetite; *Apt* apatite. See text for explanation

the eastern Yangtze craton (20–33 km depth), interpreted as reflecting basaltic underplating (Lü et al. 2004), provide further evidence for extensive partial melting of the lithospheric mantle.

Large-scaled mantle melting requires abnormally high heat flow during the early Cretaceous, which was most likely envisaged in an extensional environment. Presence of syenite, A-type granite, shoshonitic basalts, and metamorphic core complexes that have been dated between 131 and 120 Ma (Xing and Xu 1994; Wang et al. 2001; Liu et al. 2002; Grimmer et al. 2003; Wang et al. 2006; Yan et al. 2008), implies that large areas of the eastern Yangtze craton was dominated by lithospheric extension during that time period. Nevertheless, extension should have been initiated since the earliest Cretaceous or latest Jurassic, based on geochronological data of numerous mafic to acidic intrusions (Jahn et al. 1999; Xu et al. 2004; Wang et al. 2006; Yan et al. 2008). As for other regions of eastern China, such an extension event is indicated by pervasive Au–Cu–Fe–Mo mineralization (Li et al. 2003; Mao et al. 2004), wide distribution of faulted basins and metamorphic core complexes (Tian et al. 1992; Davis et al. 2002; Liu et al. 2005), and transtensional movement of the continental Tan-Lu Fault (Zhu et al. 2005). The mechanism driving the Jurassic–Cretaceous extension may have been the removal and thinning of the lithospheric mantle and upwelling of asthenosphere, as indicated by geophysical data (Chen et al. 2008) and studies of mantle-derived xenoliths sampled by Paleozoic and Cenozoic basalts (Menzies et al. 1993; Xu et al. 2000).

Conclusions

Extensive plutonic magmatism in the Daye region started in the latest Jurassic (ca. 152 Ma) and peaked in the early Cretaceous (141–132 Ma), which was followed by volcanic eruption and dyke emplacement in the 130–113 Ma interval. The plutonic rocks can be grouped as diorites and quartz diorites that show close spatial–temporal relationships. Geological, geochemical, and Sr–Nd isotopic data indicate that the diorites were formed by partial melting of enriched lithospheric mantle that had been modified by slab melts and/or fluids, followed with variable degree of olivine fractionation at mantle depth. The quartz diorites have geochemical signatures similar to adakites, which were most likely generated by fractional crystallization of an assemblage consisting of hornblende, plagioclase, magnetite, titanite and apatite, from parental dioritic magmas represented by the diorites. This study thus confirms that fractional crystallization of mantle-derived magmas may have been a more common mechanism in the formation of adakitic rocks than previously thought. The fact that voluminous magmas were emplaced broadly coevally over the eastern Yangtze craton and the eastern China continent indicates a consistent geodynamic setting responsible for their formation. A synthesis of geological, geochronological and geochemical data demonstrates that the large-scaled magmatism was driven by extensive lithospheric extension, which was most likely caused by lithosphere thinning.

Acknowledgments We acknowledge financial supports provided by Natural Science Foundation of China (grants 40334037 and 40521001), Chinese Ministry of Education (IRT0441), Chinese Ministry of Science and Technology (2007DFA21230), the 111 Project (B07039), and the CRGC grants of the University of Hong Kong. Ms. Xiao Fu and Dr. Liang Qi are thanked for major and trace elemental analyses, respectively. Drs. Yan QR, Liu XM, and Chu ZY provided expert assistance in U–Pb dating and Sr–Nd isotope analysis, respectively. We thank Drs. Haibo Zou and Qiang Wang for their insights on an early draft of the paper. Constructive reviews by Wolfgang Siebel and Joerg Geldmacher have been of considerable importance in improving the paper, for which we are very grateful. Our thanks extend to Profs. Hans Keppler and Jochen Hoefs for useful editorial suggestions.

References

Ames L, Zhou GZ, Xiong BC (1996) Geochronology and isotopic character of ultrahigh-pressure metamorphism with implications for collision of the Sino-Korean and Yangtze cratons, central China. Tectonics 15:472–489. doi:10.1029/95TC02552

Andersen T (2002) Correction of common lead in U–Pb analyses that do not report 204Pb. Chem Geol 192:59–79. doi:10.1016/S0009-2541(02)00195-X

Atherton MP, Petford N (1993) Generation of sodium-rich magmas from newly underplated basaltic crust. Nature 362:144–146. doi:10.1038/362144a0

Baker MB, Hirschmann MM, Ghiorso MS, Stolper EM (1995) Compositions of near-solidus peridotite melts from experimental and thermodynamic calculations. Nature 375:308–311. doi:10.1038/375308a0

Beard JS, Lofgren GE (1991) Dehydration melting and water-saturated melting of basaltic and andesitic greenstones and amphibolites at 1, 3, and 6.9 kb. J Petrol 32:365–401

Black LP, Kamo SL, Allen CM, Aleinikoff JN, Davis DW, Korsch RJ et al (2003) TEMORA 1: a new zircon standard for Phanerozoic U–Pb geochronology. Chem Geol 200:155–170. doi:10.1016/S0009-2541(03)00165-7

Bourdon E, Eissen JP, Monzier M, Robin C, Martin H, Cotten J et al (2002) Adakite-like lavas from Antisana volcano (Ecuador): evidence for slab melt metasomatism beneath the Andean Northern volcanic zone. J Petrol 43:199–217. doi:10.1093/petrology/43.2.199

Boynton WW (1984) Geochemistry of the rare earth element: meteorite studies. In: Henderson P (ed) Rare Earth element geochemistry: developments in geochemistry. Elsevier, Amsterdam, pp 89–92

Castillo PR, Janney PE, Solidum RU (1999) Petrology and geochemistry of Camiguin Island, southern Philippines: insights to the source of adakites and other lavas in a complex arc setting. Contrib Mineral Petrol 134:33–51. doi:10.1007/s004100050467

Castillo PR (2006) An overview of adakite petrogenesis. Chin Sci Bull 51:257–268. doi:10.1007/s11434-006-0257-7

Chang YF, Liu XP, Wu YC (1991) The copper–iron belt of the lower and middle reaches of the Changjiang River. Geological Publishing House, Beijing (in Chinese with English abstract)

Chen JF, Li XM, Zhou TX, Foland KA (1991) $^{40}Ar/^{39}Ar$ dating for the Yueshan diorite, Anhui province and the estimated formation time of the association ore deposit. Geoscience 5:91–99 (in Chinese with English abstract)

Chen L, Wang T, Zhao L, Zheng TY (2008) Distinct lateral variation of lithospheric thickness in the Northeastern North China Craton. Earth Planet Sci Lett 267:56–68

Chung SL, Liu DY, Ji JQ, Chu MF, Lee HY, Wen DJ et al (2003) Adakites from continental collision zones: melting of thickened lower crust beneath southern Tibet. Geology 31:1021–1024. doi:10.1130/G19796.1

Compston W, Williams IS, Kirschvink JL, Zichao Z, Guogan MA (1992) Zircon U–Pb ages for the Early Cambrian time scale. J Geol Soc 149:171–184. doi:10.1144/gsjgs.149.2.0171

Davis GA, Darby BJ, Zheng YD, Spell TL (2002) Geometric and temporal evolution of an extensional detachment fault, Hohhot metamorphic core complex, Inner Mongolia, China. Geology 30:1003–1006. doi:10.1130/0091-7613(2002)030>1003:GATEOA<2.0.CO;2

Deer WA, Howie RA, Zussman J (1983) An introduction to the rock-forming minerals. Longman, Hong Kong

Defant MJ, Drummond MS (1990) Derivation of some modern arc magmas by melting of young subducted lithosphere. Nature 347:662–665. doi:10.1038/347662a0

DePaolo DJ (1981) Trace element and isotopic effects of combined wall-rock assimilation and fractional crystallization. Earth Planet Sci Lett 53:189–202. doi:10.1016/0012-821X(81)90153-9

Di YJ, Wu GG, Zhang D, Song B, Zang WS, Zhang ZY et al (2005) SHRIMP U–Pb zircon geochronology of the Xiaotongguanshan and Shatanjiao intrusions and its petrological implications in the Tongling area, Anhui. Acta Geol Sin 79:795–802

Drummond MS, Defant MJ (1990) A model for trondhjemite–tonalite–dacite genesis and crustal growth via slab melting: Archean to modern comparisons. J Geophys Res 95(B):21503–21521

Falloon TJ, Green DH, O'Neill HSC, Hibberson WO (1997) Experimental tests of low degree peridotite partial melt compositions: implications for the nature of anhydrous near-solidus peridotite melts at 1 GPa. Earth Planet Sci Lett 152:149–162. doi:10.1016/S0012-821X(97)00155-6

Fan QC, Liu RX, Li HM, Li N, Sui JL, Lin ZR (1998) Zircon chronology and REE geochemistry of granulite xenoliths at Hannuoba. Chin Sci Bull 43:1510–1515. doi:10.1007/BF02883438

Faure G (1986) Principles of isotope geology. Wiley, New York

Gao S, Rudnick RL, Yuan HL, Liu XM, Liu YS, Xu WL et al (2004) Recycling lower continental crust in the North China craton. Nature 432:892–897. doi:10.1038/nature03162

Geldmacher J, Hoernle K, Klügel A, van den Bogaard P, Bindeman I (2008) Geochemistry of a new enriched mantle type locality in the northern hemisphere: implications for the origin of the EM-I source. Earth Planet Sci Lett 265:167–182. doi:10.1016/j.epsl.2007.10.001

Graviou P, Peucat JJ, Auvray B, Vidal P (1988) The Cadomian Orogeny in the northern Armorican Massif: petrological and geochronological constraints on a geodynamic model. Hercynica 1:1–13

Green DH (1973) Experimental melting studies on a model upper mantle composition at high-pressure under water-saturated and water-undersaturated conditions. Earth Planet Sci Lett 19:37–53. doi:10.1016/0012-821X(73)90176-3

Grimmer JC, Ratschbacher L, McWilliams M (2003) When did the ultrahigh-pressure rocks reach the surface? A $^{207}Pb/^{206}Pb$ zircon, $^{40}Ar/^{39}Ar$ white mica, Si-in-white mica, single-grain provenance study of Dabie Shan synorogenic foreland sediments. Chem Geol 197:87–110. doi:10.1016/S0009-2541(02)00321-2

Hofmann AW (1988) Chemical differentiation of the earth: the relationship between mantle, continental-crust, and oceanic-crust. Earth Planet Sci Lett 90:297–314. doi:10.1016/0012-821X(88)90132-X

Huang XL, Xu YG, Liu DY (2004) Geochronology, petrology and geochemistry of the granulite xenoliths from Nushan, east China: implication for a heterogeneous lower crust beneath the Sino-Korean Craton. Geochim Cosmochim Acta 68:127–149. doi:10.1016/S0016-7037(03)00416-2

Hubei Bureau of Geology, Mineral Resources (1990) Regional Geology of Hubei Province. Geological Publishing Housing, Beijing (in Chinese with English abstract)

Jackson SE, Pearson NJ, Griffin WL, Belousova EA (2004) The application of laser ablation-inductively coupled plasma-mass spectrometry to in situ U–Pb zircon geochronology. Chem Geol 211:47–69. doi:10.1016/j.chemgeo.2004.06.017

Jahn BM, Wu FY, Lo CH, Tsai CH (1999) Crust–mantle interaction induced by deep subduction of the continental crust: geochemical and Sr–Nd isotopic evidence from post-collisional mafic–ultramafic intrusions of the northern Dabie complex, central China. Chem Geol 157:119–146. doi:10.1016/S0009-2541(98)00197-1

Kay RW (1978) Aleutian magnesian andesites: melts from subducted Pacific ocean crust. J Volcanol Geotherm Res 4:117–132. doi:10.1016/0377-0273(78)90032-X

Kay RW, Kay SM (1993) Delamination and delamination magmatism. Tectonophysics 219:177–189. doi:10.1016/0040-1951(93)90295-U

Li JW, Vasconcelos PM, Zhang J, Zhou MF, Zhang XJ, Yang FH (2003) $^{40}Ar/^{39}Ar$ constraints on a temporal link between gold mineralization, magmatism, and continental margin transtension in the Jiaodong gold province, Eastern China. J Geol 111:741–751. doi:10.1086/378486

Li JW, Zhao XF, Zhou MF, Vasconcelos PM, Ma CQ (2008) Origin of the Tongshankou porphyry-skarn Cu-Mo deposit, eastern Yangtze craton, Eastern China: geochronological, geochemical, and Sr–Nd–Hf isotopic constraints. Miner Depos 43:315–336. doi:10.1007/s00126-007-0161-3

Li WX, Li XH (2003) Adakitic granites within the NE Jiangxi ophiolites, South China: geochemical and Nd isotopic evidence. Precambrian Res 122:29–44. doi:10.1016/S0301-9268(02)00206-1

Li ZX, Li XH (2007) Formation of the 1300-km-wide intracontinental orogen and postorogenic magmatic province in Mesozoic South China: a Flat-slab subduction model. Geology 35:179–182. doi:10.1130/G23193A.1

Liu H, Qiu JS, Lo CH, Xu XS, Ling WL, Wang DZ (2002) Petrogenesis of the Mesozoic potash-rich volcanic rocks in the Luzong basin, Anhui Province: geochemical constraints. Geochimica 31:129–140 (in Chinese with English abstract)

Liu JL, Davis GA, Lin ZY, Wu FY (2005) The Liaonan metamorphic core complex, Southeastern Liaoning Province, North China: a likely contributor to Cretaceous rotation of Eastern Liaoning, Korea and contiguous areas. Tectonophysics 407:65–80. doi:10.1016/j.tecto.2005.07.001

Lü QT, Hou ZQ, Zhao JH, Shi DN, Wu XZ, Chang YF et al (2004) Deep seismic reflection profiling revealing the complex crustal structure of the Tongling ore district. Sci China D 47:193–200. doi:10.1360/02YD0277

Ma CQ, Li ZC, Ehlers C, Yang KG, Wang RJ (1998) A post-collisional magmatic plumbing system: Mesozoic granitoid plutons from the Dabieshan high-pressure and ultrahigh-pressure metamorphic zone, east-central China. Lithos 45:431–456. doi:10.1016/S0024-4937(98)00043-7

Macpherson CG, Dreher ST, Thirlwall MF (2006) Adakites without slab melting: high pressure differentiation of island arc magma, Mindanao, the Philippines. Earth Planet Sci Lett 243:581–593. doi:10.1016/j.epsl.2005.12.034

Mao JW, Stein H, Du A, Zhou TH (2004) Re–Os dating of molybdenite from Cu–Au–Mo deposits in the Mid-Lower reaches of the Yangtze River belt and implication for mineralization. Acta Geol Sin 78:121–131

Martin H (1987) Petrogenesis of Archean trondhjemites, tonalites and granodiorites from eastern Finland: major and trace element geochemistry. J Petrol 28:921–953

Martin H, Smithies RH, Rapp R, Moyen JF, Champion D (2005) An overview of adakite, tonalite–trondhjemite–granodiorite (TTG), and sanukitoid: relationships and some implications for crustal evolution. Lithos 79:1–24. doi:10.1016/j.lithos.2004.04.048

McCulloch MT, Bennett VC (1994) Progressive growth of the earth's continental-crust and depleted mantle: geochemical constraints. Geochim Cosmochim Acta 58:4717–4738. doi:10.1016/0016-7037(94)90203-8

McDonough WF, Sun SS (1995) The composition of the Earth. Chem Geol 120:223–253. doi:10.1016/0009-2541(94)00140-4

Menzies M, Rogers N, Tindle A, Hawkesworth C (1987) Metasomatic and enrichment processes in lithospheric peridotites, an effect of asthenosphere–lithosphere interaction. In: Menzies MK, Hawkesworth CJ (eds) Mantle metasomatism. Academic Press Geology Series, London, pp 313–361

Menzies MA, Fan W, Zhang M (1993) Palaeozoic and Cenozoic lithoprobes and loss of 120 km of Achaean lithosphere, Sino-Korean craton, China. In: Pritchard HM, Alabaster T, Harris NBW, Neary CR (eds) Magmatic processes and plate tectonics. Geological Society, London, pp 71–81

Muir RJ, Weaver SD, Bradshaw JD, Eby GN, Evans JA (1995) The Cretaceous separation point Batholith, New Zealand: granitoid magmas formed by melting of mafic lithosphere. J Geol Soc 152:689–701. doi:10.1144/gsjgs.152.4.0689

Nicholls IA, Ringwood AE (1972) Production of silica-saturated tholeiitic magmas in island arcs. Earth Planet Sci Lett 17:243–246. doi:10.1016/0012-821X(72)90282-8

Nielsen R (2006) Geochemical Earth Reference Model (GERM) partition coefficient (Kd) database. Available at http://www.geo.oregonstate.edu/people/faculty/nielsenr.htm

Nockolds SR, Allen R (1953) The geochemistry of some igneous rock series. Geochim Cosmochim Acta 4:105–142. doi:10.1016/0016-7037(53)90055-6

Peacock SM, Rushmer T, Thompson AB (1994) Partial melting of subducting oceanic-crust. Earth Planet Sci Lett 121:227–244. doi:10.1016/0012-821X(94)90042-6

Pearce JA, Harris NBW, Tindle AG (1984) Trace-element discrimination diagrams for the tectonic interpretation of granitic rocks. J Petrol 25:956–983

Petford N, Atherton M (1996) Na-rich partial melts from newly underplated basaltic crust: The Cordillera Blanca Batholith, Peru. J Petrol 37:1491–1521. doi:10.1093/petrology/37.6.1491

Qi L, Jing H, Gregoire DC (2000) Determination of trace elements in granites by inductively coupled plasma mass spectrometry. Talanta 51:507–513. doi:10.1016/S0039-9140(99)00318-5

Rapp RP, Shimizu N, Norman MD, Applegate GS (1999) Reaction between slab-derived melts and peridotite in the mantle wedge: experimental constraints at 3.8 GPa. Chem Geol 160:335–356. doi:10.1016/S0009-2541(99)00106-0

Rapp RP, Watson EB (1995) Dehydration melting of metabasalt at 8–32-Kbar: implications for continental growth and crust–mantle recycling. J Petrol 36:891–931

Rapp RP, Watson EB, Miller CF (1991) Partial melting of amphibolite eclogite and the origin of Archean trondhjemites and tonalites. Precambrian Res 51:1–25. doi:10.1016/0301-9268(91)90092-O

Rayleigh JWS (1896) Theoretical considerations respecting the separation of gases by diffusion and similar processes. Philos Mag 42:77–107

Richards JP, Kerrich R (2007) Adakite-like rocks: their origins and questionable role in metallogenesis. Econ Geol 102:537–576. doi:10.2113/gsecongeo.102.4.537

Rollinson HR (1993) Using geochemical data: evaluation, presentation, interpretation. Wiley, New York

Rudnick RL (1995) Making continental crust. Nature 378:571–578. doi:10.1038/378571a0

Rudnick RL, Fountain DM (1995) Nature and composition of the continental crust: a lower crustal perspective. Rev Geophys 33:267–309. doi:10.1029/95RG01302

Rushmer T (1991) Partial melting of 2 amphibolites: contrasting experimental results under fluid-absent conditions. Contrib Mineral Petrol 107:41–59. doi:10.1007/BF00311184

Sajona FG, Maury RC, Bellon H, Cotten J, Defant MJ, Pubellier M (1993) Initiation of subduction and the generation of slab melts in western and eastern Mindanao, Philippines. Geology 21:1007–1010. doi:10.1130/0091-7613(1993)021>1007:IOSATG<2.3.CO;2

Sen C, Dunn T (1994) Dehydration melting of a basaltic composition amphibolite at 1.5 and 2.0 Gpa: implications for the origin of adakites. Contrib Mineral Petrol 117:394–409. doi:10.1007/BF00307273

Shaw DM (1970) Trace element fractionation during anatexis. Geochim Cosmochim Acta 34:237–243. doi:10.1016/0016-7037(70)90009-8

Shu QA, Chen PL, Chen JR (1992) Geology of Fe–Cu ore deposits in eastern Hubei Province. Press of Metallurgical Industry, Beijing (in Chinese with English abstract)

Störmer JCJ, Nicholls J (1978) XLFRAC: a program for interactive testing of magmatic differentiation models. Comput Geosci 4:143–159. doi:10.1016/0098-3004(78)90083-3

Su XD, Liu SM (1994) Application of isotopic geology to the study of Fe–Cu deposits in eastern Hubei. Geol Prospect 30:27–32 (in Chinese with English abstract)

Sun SS, McDonough WF (1989) Chemical and isotopic systematics of oceanic basalts: implications for mantle composition and processes. Geol Soc Spec Pub 42:313–345

Tatsumi Y (2006) High-Mg Andesites in the Setouchi Volcanic Belt, Southwestern Japan: analogy to Archean magmatism and continental crust formation? Annu Rev Earth Sci 34:467–499. doi:10.1146/annurev.earth.34.031405.125014

Taylor SR, McLennan SM (1985) The continental crust: its composition and evolution. Blackwell, Oxford

Tian ZY, Han P, Xu KD (1992) The Mesozoic–Cenozoic East China rift system. Tectonophysics 208:341–363. doi:10.1016/0040-1951(92)90354-9

Wang Q, Wyman DA, Xu JF, Jian P, Zhao ZH (2007) Early Cretaceous adakitic granites in the Northern Dabie Complex, central China: implications for partial melting and delamination of thickened lower crust. Geochim Cosmochim Acta 71:2609–2636. doi:10.1016/j.gca.2007.03.008

Wang Q, Wyman DA, Xu JF, Zhao ZH, Jian P, Xiong XL et al (2006) Petrogenesis of Cretaceous adakitic and shoshonitic igneous rocks in the Luzong area, Anhui Province (eastern China): implications for geodynamics and Cu–Au mineralization. Lithos 89:424–446. doi:10.1016/j.lithos.2005.12.010

Wang Q, Zhao ZH, Bao ZW, Xu JF, Liu W, Li CF et al (2004) Geochemistry and petrogenesis of the Tongshankou and Yinzu adakitic intrusive rocks and the associated porphyry copper–molybdenum mineralization in southeast Hubei, east China. Resour Geol 54:137–152

Wang YL, Zhang Q, Wang Y (2001) Geochemical characteristics of volcanic rocks from Ningwu area, and its significance. Acta Petrol Sin 17:565–575 (in Chinese with English abstract)

Whalen JB, Jenner GA, Longstaffe FJ (1996) Geochemical and isotopic (O, Nd, Pb and Sr) constraints on A-type granite petrogenesis based on the Topsails Igneous Suite, Newfoundland Appalachians. J Petrol 87:1463–1489. doi:10.1093/petrology/37.6.1463

Wareham CD, Millar IL, Vaughan APM (1997) The generation of sodic granite magmas, western Palmer Land, Antarctic Peninsula. Contrib Mineral Petrol 128:81–96. doi:10.1007/s004100050295

Wilde SA, Zhou XH, Nemchin AA, Sun M (2003) Mesozoic crust–mantle interaction beneath the North China craton: a consequence of the dispersal of Gondwanaland and accretion of Asia. Geology 31:817–820. doi:10.1130/G19489.1

Wilson M (1989) Igneous petrogenesis: a global tectonic approach. Chapman & Hall, London, p 466

Workman RK, Hart SR (2005) Major and trace element composition of the depleted MORB mantle (DMM). Earth Planet Sci Lett 231:53–72. doi:10.1016/j.epsl.2004.12.005

Wu CL, Zhou XR, Huang XC, Zhang CH, Huang WM (1996) 40Ar/39Ar chronology of intrusive rocks from Tongling. Acta Petrol Miner 15:299–306 (in Chinese with English abstract)

Wu FY, Lin JQ, Wilde SA, Zhang XO, Yang JH (2005a) Nature and significance of the Early Cretaceous giant igneous event in eastern China. Earth Planet Sci Lett 233:103–119. doi:10.1016/j.epsl.2005.02.019

Wu FY, Yang JH, Wilde SA, Zhang XO (2005b) Geochronology, petrogenesis and tectonic implications of Jurassic granites in the Liaodong Peninsula, NE China. Chem Geol 221:127–156. doi:10.1016/j.chemgeo.2005.04.010

Wu LS, Zhou XQ (1997) Re–Os isotopic dating of the Chengmenshan copper deposit, Jiangxi Province. Miner Depos 16:376–381 (in Chinese with English abstract)

Xie GQ, Mao JW, Li R, Zhou SD, Ye HR, Yan QR et al (2006) SHRIMP U–Pb age of the Dasi Formation volcanic rocks from southeastern Hubei, mid-lower reaches of the Yangtze River. Sci China D 51:2283–2291

Xie JC, Yang XY, Du JG, Sun WD (2008) Zircon U–Pb geochronology of the Mesozoic intrusive rocks in the Tongling region: implications for Cu–Au mineralization. Acta Petrol Sin (in press)

Xing FM, Xu X (1994) Two A-type granite belts from Anhui. Acta Petrol Sin 10:357–369 (in Chinese with English abstract)

Xing FM, Xu X (1996) High-potassium calc-alkaline intrusive rocks in Tongling area, Anhui province. Geochimica 25:29–38 (in Chinese with English abstract)

Xu HJ, Ma CQ, Ye K (2007) Early Cretaceous granitoids and their implications for the collapse of the Dabie orogen, eastern China: SHRIMP zircon U–Pb dating and geochemistry. Chem Geol 240:238–259. doi:10.1016/j.chemgeo.2007.02.018

Xu JF, Shinjo R, Defant MJ, Wang Q, Rapp RP (2002) Origin of Mesozoic adakitic intrusive rocks in the Ningzhen area of east China: partial melting of delaminated lower continental crust? Geology 30:1111–1114. doi:10.1130/0091-7613(2002)030>1111:OOMAIR<2.0.CO;2

Xu X, Xing FM (1994) Whole-rock and mineral Rb–Sr isochron ages of the three gabbros in Nanjing–Wuhu Area, China. Sci Geol Sin 29:309–312 (in Chinese with English abstract)

Xu XS, O'Reilly SY, Griffin WL, Zhou XM (2000) Genesis of young lithospheric mantle in southeastern China: an LAM-ICPMS trace element study. J Petrol 41:111–148. doi:10.1093/petrology/41.1.111

Xu YG, Huang XL, Ma JL, Wang YB, Iizuka Y, Xu JF et al (2004) Crust–mantle interaction during the tectono-thermal reactivation of the North China Craton: constraints from SHRIMP zircon U–Pb chronology and geochemistry of Mesozoic plutons from western Shandong. Contrib Mineral Petrol 147:750–767. doi:10.1007/s00410-004-0594-y

Yan J, Chen JF, Xu XS (2008) Geochemistry of Cretaceous mafic rocks from the Lower Yangtze region, eastern China: characteristics and evolution of the lithospheric mantle. J Asian Earth Sci 33:177–193. doi:10.1016/j.jseaes.2007.11.002

Yang ZY, Cheng YQ, Wang HZ (1986) The Geology of China. Oxford University Press, New York

Yu JH, Xu XS, O'Reilly SY, Griffin WL, Zhang M (2003) Granulite xenoliths from Cenozoic Basalts in SE China provide geochemical fingerprints to distinguish lower crust terranes from the North and South China tectonic blocks. Lithos 67:77–102. doi:10.1016/S0024-4937(02)00253-0

Yuan HL, Gao S, Liu XM, Li HM, Gunther D, Wu FY (2004) Accurate U–Pb age and trace element determinations of zircon by laser ablation-inductively coupled plasma-mass spectrometry. Geostand Geoanal Res 28:353–370. doi:10.1111/j.1751-908X.2004.tb00755.x

Zhai YS, Xiong YL, Yao SZ, Lin XD (1996) Metallogeny of copper and iron deposits in the Eastern Yangtse Craton, east-central China. Ore Geol Rev 11:229–248. doi:10.1016/0169-1368(96)00003-0

Zhai YS, Yao SZ, Lin XD, Zhou XR (1992) Metallogeny of Fe–zCu–(Au) ore deposits in mid-lower Yangtze River. Geological Publishing House, Beijing (in Chinese with English abstract)

Zhou XM, Li WX (2000) Origin of Late Mesozoic igneous rocks in Southeastern China: implications for lithosphere subduction and underplating of mafic magmas. Tectonophysics 326:269–287. doi:10.1016/S0040-1951(00)00120-7

Zhu G, Wang YS, Liu GS, Niu ML, Xie CL, Li CC (2005) $^{40}Ar/^{39}Ar$ dating of strike-slip motion on the Tan-Lu fault zone, East China. J Struct Geol 27:1379–1398. doi:10.1016/j.jsg.2005.04.007